Fall 12-2020

Numerical Analysis of a Roadway Piezoelectric Harvesting System

Abdul Rahman Badawi
Old Dominion University, abdulrahmanbadawi@hotmail.com

NUMERICAL ANALYSIS OF A ROADWAY PIEZOELECTRIC HARVESTING SYSTEM

by

Abdul Rahman Badawi
B.S. August 2018, Hashemite University, Jordan
M.S. December 2020, Old Dominion University

A Thesis Submitted to the Faculty of
Old Dominion University in Partial Fulfilment of
Requirements for the Degree of

MASTER OF SCIENCE

MECHANICAL & AEROSPACE ENGINEERING

OLD DOMINION UNIVERSITY
December 2020

Approved by:

Tian-Bing Xu (Chair)

Mileta Tomovic (Member)

Arthur Taylor (Member)

ABSTRACT

NUMERICAL ANALYSIS OF A ROADWAY PIEZOELECTRIC HARVESTING SYSTEM

Abdul Rahman Badawi
Old Dominion University, 2020
Director: Dr. Tian-Bing Xu

Highways, streets, bridges, and sidewalks with heavy traffic dissipate a considerable amount of waste mechanical energy every day. Piezoelectric energy harvesting devices are a very promising technology that can convert the waste mechanical energy to clean and renewable energy to enhance the sustainability of infrastructures. Research efforts in large-scale energy harvesting have led to the advancement of piezoelectric devices to the point that large-scale implementation is starting to become more feasible. The energy harvested by these devices can be used in many ways such as providing heating or cooling, melting ice, monitoring structural conditions in bridges and tunnels, and powering wireless sensors. Additionally, these devices contain an off-grid power system meaning that it has a standalone battery connected to it. This is highly beneficial in areas where city power sources are not readily available. The objective of this thesis is to study the energy harvesting potential of a dual-mode piezoelectric generator to develop a roadway piezoelectric harvesting system with ultra-high-power density and efficiency.

The dual-mode harvester is made up of APC 855 with two different modes, 33-mode and 15-mode. In order to structurally optimize the design, finite element analysis was performed using ANSYS Mechanical and APDL. Static and transient simulations for each model with detailed input conditions were evaluated to determine the optimal configuration. Two different vehicle sizes were evaluated to assess the load effect on the harvested power. In addition, open circuit and closed-circuit models with different resistance values were compared to determine the resistance that

produces the highest energy. Furthermore, a comparison between the different polarization directions for the 15-mode harvester was investigated to determine the optimal polarization direction.

To my family.

ACKNOWLEDGEMENTS

First and foremost, all praise to be Allah almighty, the most merciful and most giving, for the endless blessings and guidance he has provided. During the course of this work, Dr. Tian-Bing Xu has offered a substantial amount of dedication and effort. I would like to express my utmost sincere gratitude to him. I would like to thank him for the long days and nights he spent during meetings and calls to assist in getting this project where it is. I am deeply honored to be one of his students. I would also like to thank Dr. Bawab and the Mechanical Engineering department for funding my education and giving me a chance to prove myself as graduate teaching assistant.

My utmost respect and gratitude must be paid to Mohammad Shabara, my friend and colleague, for spending countless hours by my side assisting me in my simulations, providing me with invaluable knowledge, giving me expert advice on how to better myself, and being patient with me this whole time. I am extremely grateful for everything he has done and can not repay him with all the words in the world.

My journey at Old Dominion University would have never been this great without the help and support of my Uncle Usama, his wife, Ameera, and his children. They have been like a second family to me and made my time away from family and home bearable.

Last but not least, I would like to express my profound gratitude for my family. I owe everything to the unconditional love and support that was provide by my parents, Elham and Isam. To the encouragement of my brother Mohaned, and the continuous love and support of my sisters, Rawand and Layan.

NOMENCLATURE

σ	Stress
D	Electric Displacement Vector
d_{33}	Piezoelectric Constant “C/N”
d_{ij}	Piezoelectric Charge Constant
e_{ij}	Piezoelectric Stress Coefficient
F	Force
f	frequency “Hz”
L	Length of the Stack
p	Number of Piezoelectric Layers
t_p	Layer Thickness
Q	Electric Charge “Coulomb”
R	Electric Resistance “Ohm”
S	Strain
s_{ij}^{E}	Compliance Coefficient
t	Time “sec”
V	Voltage “Volts”
Y	Young’s Modulus of Elasticity
PEH	Piezoelectric Energy Harvesters

TABLE OF CONTENTS

CHAPTER PAGE

CHAPTER PAGE

LIST OF TABLES

LIST OF FIGURES

Figure Page

Figure Page

Figure Page

Figure Page

I. INTRODUCTION

The word “piezo” is derived from the Greek language, meaning “to press.” In 1880, Pierre and Jacques Curie also known as the Curie brothers were the first to discover piezoelectricity [1]. They found that in specific materials such as quartz, zincblende, and topaz, macroscopic polarization and electric charges were produced when these materials were subjected to mechanical stresses. A year later, Lippman, predicted the reverse piezoelectric effect relying on thermodynamic considerations [2]. He predicted that an imposed voltage produces mechanical deformations or strains the material. It took approximately 40 years, in the 1920’s for the first application of piezoelectricity to be invented. Piezoelectricity in quartz was employed to realize crystal resonators for the stabilization of oscillators, thus initiating the field of frequency control [3]. Following the discovery of quartz control, man-made piezoelectric materials broadened the field of devices and applications such as sonar systems, microphones, accelerometers, and ultrasonic transducers. Today, piezoelectric applications are used in smart materials for vibration control, aerospace applications of flexible structures, energy harvesters, and sensors for robotic applications [4].

Electric Polarization and Types of Materials

When an external electric field is applied to a solid, the solid adjusts to this agitation by changing the positions of the electrons and nuclei. As a result, dipoles are generated, and the material is said to experience polarization. The alignment process of the already existing permanent or induced atomic molecular dipoles subjected to an external electric field that has a field strength, E, is called polarization. There are three main types of polarization: ionic, electronic, and dipolar polarization. For an AC electric field, the frequency of the applied field is the main

factor that contributes to the degree of which each polarization mechanism affects the overall polarization, as shown in Fig. 1. Hence, each mechanism stops functioning when the applied field frequency surpasses its relaxation frequency [4].

Electronic polarization may be applied to one degree or another in all atoms of a material. It is the result of the displacement of the center of the negatively charged electron cloud relative to the positive nucleus of an atom by the electric field, as illustrated in Fig. 1. This type of polarization is found in all dielectric materials and exists only while an electric field is present [4]. Ionic materials are the only materials that experience ionic polarization. An applied field displaces anions in one direction and cations in the opposite direction, which results in a net dipole moment, see the right-center of Fig. 1. The third and final type of polarization is dipolar, it is found only in materials that possess a permanent dipole moment. The polarization develops from a rotation in the permanent moments into the direction of the applied field, top-right of Fig.1[4].

The overall polarization of a body is equal to the sum of the ionic, dipolar, and electronic polarizations. It is possible that one or more of these mechanisms to be deficient or negligible in weight relative to others. Equation. 1 represents the average polarization per unit volume, $\vec{P}$, produced by N electric dipole moment, $\vec{p}$ which are all aligned [4].

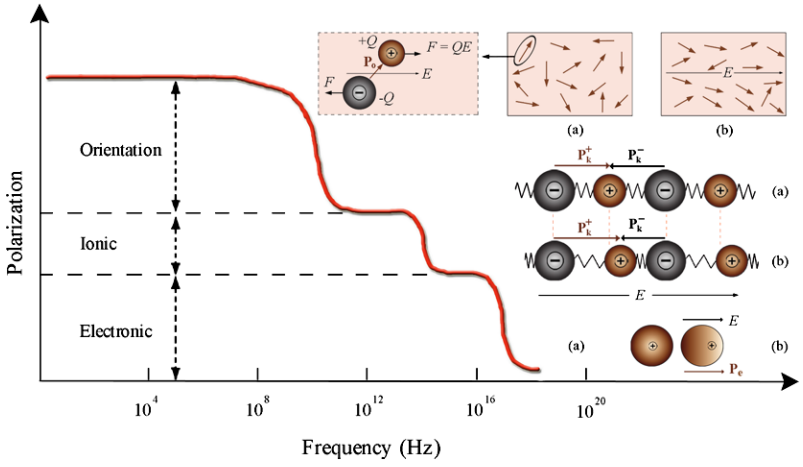

Figure 1. Frequency dependence of the electronic, ionic, and dipolar polarization mechanisms [4]

$$\vec{P} = \frac{1}{Volume}\sum_{k=0}^{N}\vec{p}_k \quad (1)$$

DIELECTRIC MATERIALS

Dielectric materials are materials that are electrically insulating (nonmetallic) and exhibit or can be made to exhibit an electric dipole structure. This means that there is a separation of negative and positive electrically charged entities on an atomic or molecular level. In general, dielectric materials exhibit at least one of the polarization types examined in the previous section. They mainly depend on the type of material and the method that the external field is applied. There are two types of dielectrics, polar and nonpolar. Polar dielectrics are dielectrics that have permanent electric dipole moments. As shown in the top right of Fig. 1, the polar molecules are randomly oriented in the absence of an external field. When an external electric field *E* is applied, a torque appears and causes the molecules to align with the field. Then again, the molecules aren't perfectly aligned due to random thermal motion. Nonpolar dielectrics are dielectrics that do not have permanent dipole moment. Electric dipole moments can be stimulated by placing the materials in an externally applied electric field, see Fig 1. Even though dielectrics are electrically insulating, they are vulnerable to polarization when an electric field is applied. Therefore dielectrics have the ability to increase the charge storing capability of capacitors; the dielectric constant is the efficiency of this ability [4].

PIEZOELECTRIC MATERIALS

Piezoelectric materials are a division of dielectrics which can be polarized, in addition to generate an electric field by applying a mechanical stress Fig. 2. This phenomenon which is uncommonly exhibited by a few dielectrics is called piezoelectricity, or plainly, pressure electricity. Since piezoelectrics are a division of dielectric materials, they can also be polar (contain a net dipole moment) and nonpolar (sum of dipole moments in different directions is zero) [4]. The following sections will provide an in-depth description of the piezoelectric effect.

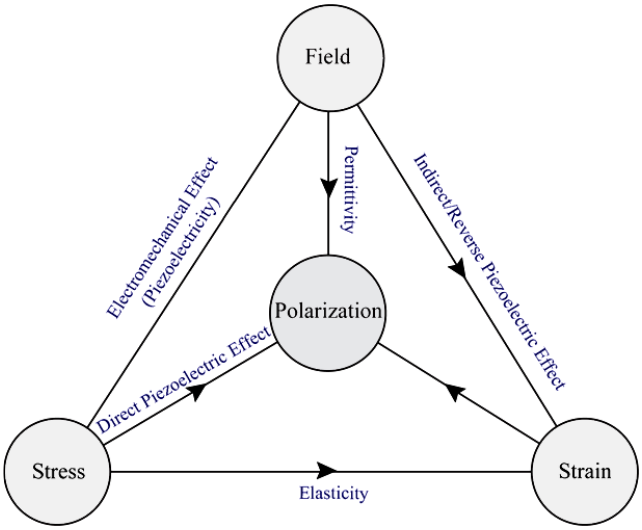

Figure 2. The correlation between stress, strain, electric field, and polarization in piezoelectric materials [4]

THE PIEZOELECTRIC EFFECT

Regular crystals in materials are described by how their atoms are oriented in a specific structure held together by bonds, this is called a unit cell. Most crystalline materials such as iron have crystals that are symmetric which render them useless for use as piezoelectrics. However, some materials such as quartz have a crystalline structure that is asymmetric but still exist in an

electrically neutral balance. If mechanical stress is applied to this piezoelectric crystal, the structure deforms which produces an electrical charge as seen in Fig. 3. This is called the direct piezoelectric effect. If we take the same crystal and apply an electric current to it, the crystal will contract or expand, converting electrical energy into strain. This is called the indirect piezoelectric effect.

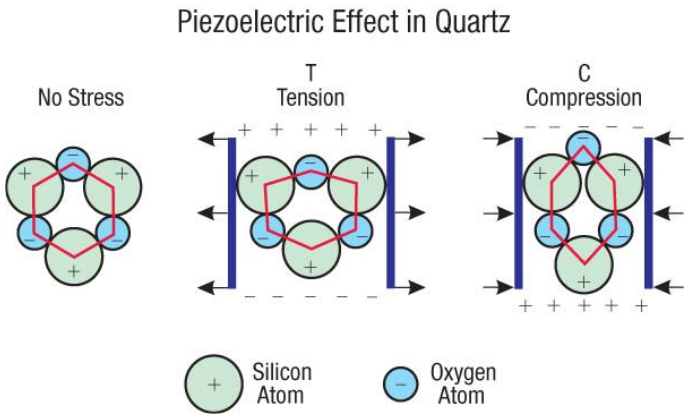

Figure 3. Effect of Tension and Compression on the electric charge produced in Quartz

Piezoelectric Coefficients [5]

Since piezoelectric materials are anisotropic, physical constants relate to both the direction of the electric field or applied mechanical stress and the directions perpendicular to the applied load. Accordingly, as illustrated in the previous section, each coefficient generally has two subscripts that specify the directions of the two related quantities, such as stress (the direction force applied on the material's surface area) and strain (the change in length of the material) for elasticity. Fig. 4 illustrates the direction of forces affecting a piezoelectric element [6]. These physical constants will be discussed here in more detail.

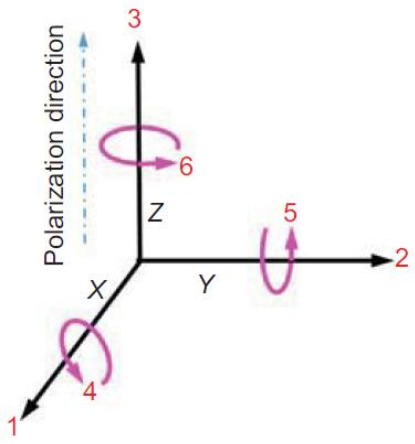

Figure 4. Axis directions nomenclature [6]

Piezoelectric charge constant ($\boldsymbol{d_{ij}}$)

The piezoelectric charge constant, d_{ij}, represents the electric charged produced per unit of mechanical stress applied to a piezoelectric element, or, alternatively, it is the mechanical strain that results in a piezoelectric material per unit of applied electric field. The first subscript "*i*" specifies the direction of polarization produced in the piezoelectric element when the electric field, *E*, is 0, or alternatively, the direction of the applied field strength. The second subscript "*j*" is the direction of the induced strain or applied stress in the material [6]. Fig. 5 shows a voltage *V* being applied to a piezoelectric transducer which is polarized in the 3 direction.

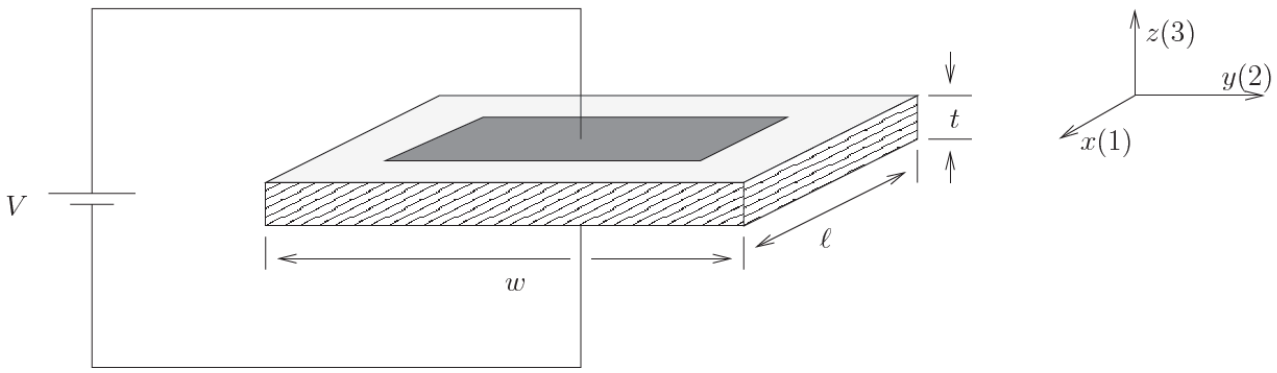

Figure 5. d_{31} arrangement for a piezoelectric transducer [7]

The applied voltage in the 3 direction generates an electric field

$$E_3 = \frac{V}{t} \tag{2}$$

which strains the transducer particularly in the 1 direction

$$\varepsilon_1 = \frac{\Delta l}{l} \tag{3}$$

where

$$\Delta l = \frac{d_{31} V l}{t} \tag{4}$$

This is for the indirect piezoelectric effect. For the direct piezoelectric effect, where the stress applied generates a voltage, we have a force *F* applied in the 3 direction to generate a stress

$$\sigma_3 = \frac{F}{lw} \tag{5}$$

which results in the electric charge

$$q = d_{33}F \tag{6}$$

If the stress is applied in all 3 directions equally, and the direction of the electrodes is perpendicular to the 3 axis, the short-circuit charge per unit of applied stress is represented by d_p [7].

Piezoelectric voltage constant $(\boldsymbol{g_{ij}})$

The electric field generated by a piezoelectric element per unit of mechanical stress applied is called the piezoelectric voltage constant. Alternatively, it is defined as the mechanical strain induced in a piezoelectric material per unit of applied electric displacement. The first subscript "i" specifies the direction of the electric field generated in the material or the direction of applied electrical displacement. The second subscript "j" indicates the direction of the applied stress or induced strain, respectively. The Piezoelectric voltage constant is important for assessing how suitable a material is to be used as a sensor or energy harvester in various applications [6].

For a piezoelectric material that has a piezoelectric voltage constant g_{31}, the applied force *F*, results in the voltage

$$V = \frac{g_{31}F}{w} \tag{7}$$

and if an electric charge of Q flows through the surface electrodes, the thickness of the element will change by

$$\Delta l = \frac{g_{31}Q}{w} \tag{8}$$

Permittivity ($\boldsymbol{\xi_{ij}}$)

The dielectric constant or, permittivity, ξ_{ij}, in a piezoelectric material is the dielectric displacement per unit electric field. ξ^{σ}, is the permittivity measured at a constant stress. It can also be measured at constant strain. The first subscript "*i*", specifies the direction of the dielectric displacement. The second subscript "*j*" represents the direction of the electric field. One important constant is ξ_0, which is the charge that can be stored by the same set of electrodes that are in a system, when they are separated by a vacuum, at equal voltage [6].

Elastic compliance ($\boldsymbol{S_{ij}}$)

Elastic compliance in piezoelectrics is the induced strain in the material per unit stress, and for the 11 and 33 directions, it is the reciprocal of the Young's modulus *Y*. S^E represents the compliance measured at constant electric field and $S^D$is the compliance measured at constant electrical displacement. Subscript "*i*" represents the direction of the strain, and "*j*" represents the direction of the stress [6]. Indices 1, 2, and 3 indicate compressive or tensile strains and stresses. While indices 4, 5, and 6, represent shear strains and stresses.

Piezoelectric coupling coefficient ($\boldsymbol{k_{ij}}$)

The piezoelectric coupling coefficient k_{ij} indicates the effectiveness of a piezoelectric material in transforming electrical energy to mechanical energy or mechanical to electrical energy. This transformation of energy is utilized both in piezoelectric actuators and sensors. Subscript "*i*" denotes the direction along which the electrodes are applied, and "*j*" represents the direction of the mechanical stress applied or developed. The piezoelectric coupling coefficient assumes no dielectric or mechanical losses [6,7].

II. LITERATURE REVIEW

PIEZOELECTRIC MATERIALS

Piezoelectric materials are considered a subcategory from the so called "smart materials." Smart materials are materials that can respond to an input applied to it in the form of stress, electric field, magnetic field, heat or light with an output in the form of strain, magnetization, charge, current, temperature, or light as defined in Uchino [8],the electric-mechanical (E-M) energy conversion effect is called piezoelectric effect. Piezoelectric materials can be further classified into non-organic piezoelectric materials (piezoceramics) and organic piezoelectric materials (piezopolymers). As mentioned in the introduction the piezoelectric effect was first discovered by the French physicist brothers

Jacques and Pierre Curie discovered in quartz in 1880. From that time, no significant discovery was reported until 1946 when Barium Titanate "$BaTiO_3$" was discovered, it is considered the first developed piezoceramic [9,10]. Depending on the temperature of operation, the "$BaTiO_3$" has two forms - ferroelectric and non-ferroelectric - separated by the so-called Curie temperature. The discovery of the Barium Titanate was a breakthrough in the smart materials field due to its unprecedented high electro-mechanical coupling factor [11], which at that time opened the door for more piezoelectric discoveries. In 1954 Jaffe et al. [12] discovered the inorganic perovskite compounds named lead zirconate titanate ceramics (PZT); currently, the coupling factor of the PZT ceramics can reach as high as 75%.

In the 1960, the lead-free PZT ceramics were discovered Bismuth Sodium Titanate (BNT) [13] which is also an inorganic compound that conforms with the perovskite structure. The perovskite structure is named after the Russian mineralogist L. A. Perovski[14]. A perovskite structure is defined as a crustal that has anion atoms (ions with extra electrons $-ve$) in their corners

(in our case its Oxygen atoms) and they follow the formula ACX_3, where A and B atoms resemble the cation (ions with lesser electrons −v*e*) with different sizes; usually A atoms are larger than B atoms [15]. With the beginning of the 21st century further advancements and innovation were done in field of piezoelectric materials that lead to the development KNN, BT, BNT, BFO based ceramics.

In the last 3 decades, great efforts on developing relaxor piezoelectric signal crystal materials such as $Pb(Mg_{1/3}Nb_{2/3})1\text{-}xTixO_3$ (PMN-PT) [16] [17], $Pb(In_{1/2}Nb_{1/2})O_3–Pb(Mg_{1/3}Nb_{2/3})O_3–PbTiO_3$ (PIN-PMN-PT), $Pb(Zn_{1/3}Nb_{2/3})O_3PbTiO_3$ (PZN-PT), which have significant advantages over the common piezoelectric ceramic [18]. The electromechanical coupling effects as high as 96% and the piezoelectric ecoefficiency as high as 3500. Since Kawai discovered strong piezoelectric effect in poly(vinylidene fluoride) (PVDF), various piezoelectric polymeric materials, such as Poly(vinylidenefluoride-trifluoroethylene) P(VDF-TrFE) copolymer [18] [19], poly(vinylidene fluoride-trifluoroethyleneclorotrifluoroethylene) [P(VDF-TrFE-CTFE)] terpolymer [20], odd nylons, polyamides [21], and polymeric composites.

In-organic materials classification and theory of operation

Inorganic piezoelectric materials are conventionally divided into two types, piezoelectric ceramics (polycrystal) and piezoelectric crystals. The term *crystal* according to the IEEE standard [22] is only applied to solids whose atoms arrangements are repeated in a single and consistent manner throughout the whole continuum domain. And for a crystal structure to be considered piezoelectric it must have the following two properties:

1) The crystal lattice must contain polar bonds which means that some atoms (ions) in the lattice have different charges.

2) Piezoelectric materials have non-centrosymmetric crystalline form as shown in Fig. (6a), i.e. the crystal lattice is not symmetric.

An example of this is the quartz crystal, quartz consists of a continuous framework of SiO_4 tetrahedrons, the Quartz chemical formula is SO_2 as each oxygen atom is shared between 2 tetrahedrons [23], the oxygen has negative charge and the silicon has positive charge. When the material is unloaded (either mechanical or electrical), the center of negative charges (from *O*) co-onside on the center of the positive charges (from the *Si*) as shown in Fig. (6a). When force is applied along the axis of symmetry, the center of positive and negative charges will be displaced as shown which creates free charges that can be used.

Table 1. Crystallographic Classification

<table>
<tr><th colspan="5">32 Crystalline classes</th></tr>
<tr><td colspan="4">21 non-centrosymmetric</td><td>11
centrosymmetric</td></tr>
<tr><td colspan="3">20 Piezoelectric</td><td>Gyroidal
Class 432</td><td>Non-piezoelectric</td></tr>
<tr><td colspan="2">10 Classes Pyroelectric</td><td>Non-Pyroelectric</td><td></td><td></td></tr>
<tr><td>Ferroelectric</td><td>Non-Ferroelectric</td><td></td><td></td><td></td></tr>
</table>

In crystallography, there are only 32 crystal classes "geometric classes" [9], [24], 21 of these 32 classes experience the piezoelectric phenomenon [25], a piezoelectric material has to have an asymmetric crystal lattice structure or a non-centrosymmetric crystalline form Table (1).

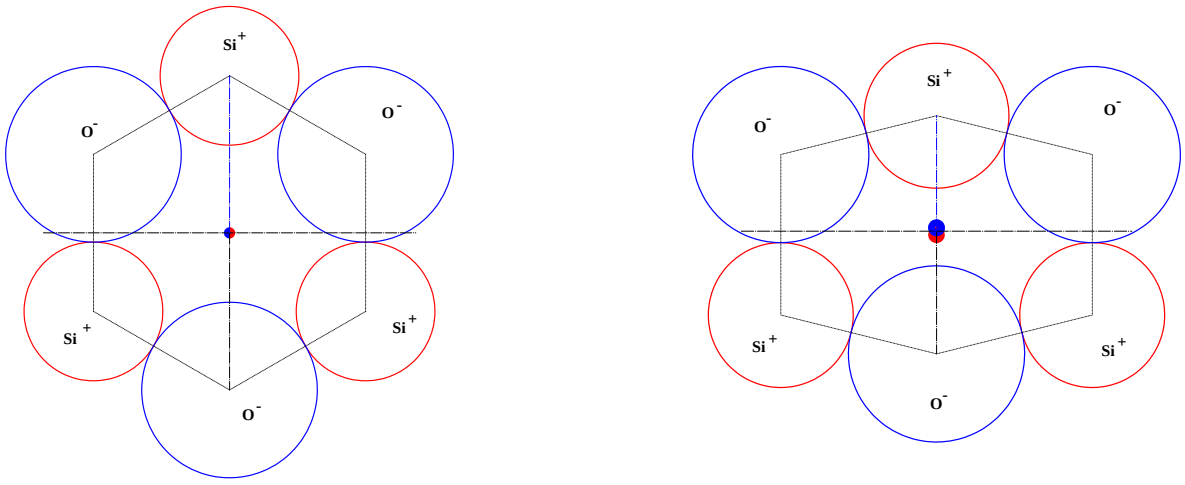

(a) Quartz crystal under no load condition **(b) Quartz crystal after applying load on it**

Figure 6. Quartz Crustal structure schematic

Lead zirconate titanate (PZT) ceramic is one of the most popular piezoelectric materials due to its high dielectric constant, high piezoelectric coefficient, and relative broad operation temperature. Piezoelectric PZT can be used in the temperature from -100 $^{\circ}C$ to 350 $^{\circ}C$. Piezoceramics (PZT) can be also classified to classification soft, semi-hard and hard ceramics depending on the composition of the ceramic, the soft ceramics has a donor dopant while the hard ceramic has an acceptor dopant. Dopants (also known as doping agents) in crystallography are impurities that are added to the crystalline structure to impose some changes in their electrical or optical characteristics. A comparison between the types of PZT mentioned above can be found in Table (2). Uchino [26] work, he thoroughly explained the material fabrication, manufacturing and processes as well as material selection and the effect of dopants addition as well as other manufacturing aspects.

Relaxor piezoelectric signal crystal PMN-PT, PIN-PMN-PT, PZN-PT , have significant higher a) electromechanical coupling effects (> 90%), b) piezoelectric ecoefficiency (> 2000pC/N), and excellent cryogenic properties (done to -230 $^{\circ}C$), [27][28] in comparison with PZT materials. However, the cost of these single crystal materials is still one order of magnitude higher than PZT materials. Only special space applications might be considered.

For high temperature piezoelectric materials, such as the commercialized Lithium niobate (LiNbO3, LN) and newly developed, rare-earth calcium oxyborate crystals [ReCa4O(BO3)3, ReCOB, Re: rare-earth] can be operated up to 1000° C [29]. Principally, piezoelectric ceramic and single crystal inorganic materials can make different harvesters to be operated from -230 $^{\circ}C$ to 1000 $^{\circ}C$.

A piezoelectric material is strongly directional dependent. The two common modes of piezoelectric operation are shown in Fig. (7). When the applied mechanical load/force is perpendicular to the dipole moment direction as shown in Fig. (7a), it is called "31" (or transverse) mode. When the applied mechanical load/force is parallel to the dipole moment direction as shown in Fig. (7b), it is called "33" (or longitudinal) mode [30]. For most piezoelectric

Table 2. Material Properties of Some PZT Ceramics [31], [32]

Property	**Soft PZT**	**Semi-Hard PZT**	**Hard PZT**
E-M Coupling factor	High	Medium	Low
Piezoelectric Coefficient	High	Medium	Low
Permittivity	High	Medium	Low
tan(δ)	High	Medium	Low
Elastic Compliance	High	Medium	Low
*Q*m	Low	Medium	High
Density	Low	Medium	High
T_c	Low	Medium	High
Polarization	Bad	Medium	Better

materials, the piezoelectric coefficient, which is the produced electrical charge over applied force, in "33" mode is twice its value in "31" mode. Furthermore, the energy conversion efficiency in a "33" mode harvester is 3-5 times higher than compared to a "31" mode harvester of same material and operating condition. However, "31" mode is more popular used for device application because it is easier and cheaper to manufacture. This is one major reason that the energy harvesting efficiency of current technology is still relatively lower.

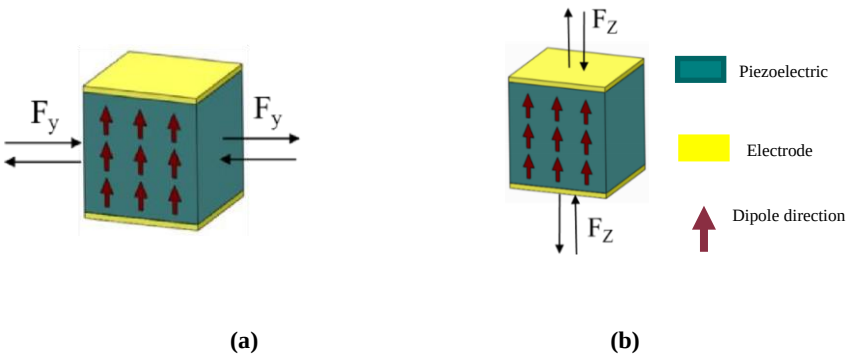

Figure 7. Diagram of (a) 31 Mode (b) 33 Mode [33]

Table 3. Examples of Piezoceramics

Property	**Quartz** [34,35]	$BaTiO_3$ [32]	**PZT** [33,36]	**PMN-PT, PZN-PT** [37–40]
ε	3.82 ~ 5	1700	425-4000	4000 ~ 9000
d_{33} pC/N	2.3	149	-600 ~ -100	1400 ~ 3500
d_{31} pC/N	0.93	-60	-276 ~ -95	-2600 ~ -900
k_{33}(%)	9	21	30 ~ 75	84 ~ 94
Y (GPa)	102.8	120	59 ~ 90	10 ~ 30
Q_m	$> 10^5$	1300	65 ~ 1400	
T_c $°C$	573	120	-150 ~ 250	130 ~ 166

Organic Piezoelectric Polymeric Materials

Examples of commonly used properties of piezoelectric polymers are listed in Table 4. In order to make piezoelectric polymer with piezoelectric properties, i.e. aligned permanent polarization, the following processing [19,41,42] are commonly required 1) stretching (biaxially

or uniaxially) the films to align chemical chains along a certain direction; 2) annealing to increase crystallinity; and 3) poling electrically to align dipoles to a certain direction. The stretching to align the chemical chain processing make the elastic modulus and electromechanical coupling factor higher along the stretched direction(s) in comparison with the thickness direction of the film. Therefore, d_{31} mode piezoelectric energy harvesters will have relatively higher energy conversation efficiencies. In addition, electromechanical coupling factor is also strongly dependent on DC bias field [42]. The advantages of piezoelectric polymer that lightweight, flexible, acoustic impedance is compatible with human body, lead-free, and larger deformation [19,43] make piezoelectric polymer harvesters more suitable for human motion energy harvesting. Although piezoelectric ecoefficiency of is lower than PZT, it is attractive to be used for medical applications. Recently, PolyK technologies (http://polyk-lab.com) made large quantity and high quality of commercial piezoelectric PVDF, P(VDF-TrFE) copolymer, and PVDF-TrFE-CFE & CTFE terpolymer films.

Table 4. Examples of commonly used properties of piezoelectric polymers

Materials		**Modulus (*GPa*)**	$d_{31}(pC/N)$	$d_{33}(pC/N)$	k_{31}%	Reference
Poly(vinylidene fluoride) (PVDF)	Biaxially stretched	2.5	4.34	-12.4		[41]
	Uniaxially stretched	2.5	21.4	-32.5	13	
Poly(vinylidenefluoride-trifluoroethylene) P(VDF-TrFE)		2.2	>25	>25	25	http://polyklab.com/taxonomy/term/7
Nylon-11			3 @25°*C* & 14 @150°*C*		4.9	[41]

PIEZOELECTRIC HARVESTING DEVICES

In this section we discuss the PEH main types, the harvester should withstand the cyclic high stress and fatigue loading applied on it. The harvesters operating in the resonance frequency produces more power compared to the off-resonance mode, that made the mechanical stability on of the main factors for the transducer selection.

Cantilever Based Energy Harvesters

Most rigid body dynamical systems are subjected to vibrations that can be caused by various factors such as, wear and tear of materials or unbalanced mass. Each system behaves differently, and the characteristic behavior of this system can be described by two parameters: the

natural frequency of the system and the damping constant. In energy harvesting, we can employ a single degree of freedom mass-spring system to study the dynamic characteristics of a vibrating body. This helps us study the unidirectional response of the system [44] [45]. The most widespread configuration in piezoelectric energy harvesting is the cantilever beam [6]. The figure below shows a diagram of a cantilever based PEH.

Figure 8. Basic cantilever based PEH configuration

As depicted in the Fig. (8), the cantilever beam is fixed to the vibration source. A proof mass is attached to the cantilever beam in order to reduce the sensitivity to the change in frequency of the system. Without the proof mass, the cantilever beam would have a high mechanical quality factor which would cause the oscillation amplitude to rapidly drop as the excitation frequency deviates from the resonance frequency of the system. Furthermore, the overall mechanical energy stored in the system is increased due to the proof mass. However, this may negatively impact the mechanical and electrical energy conversion efficiency of the cantilever-mass PEH [6]. The two main advantages of this type of PEHs are the large mechanical strains that can be generated in the material as a response to applied small forces and the more notable advantage is that the resonant frequency of a cantilever is much lower compared to other configurations. These characteristics

make the cantilever beam the most used PEH. Moreover, cantilever PEHs take two major forms, unimorph and bimorph straight cantilevers [45–47].

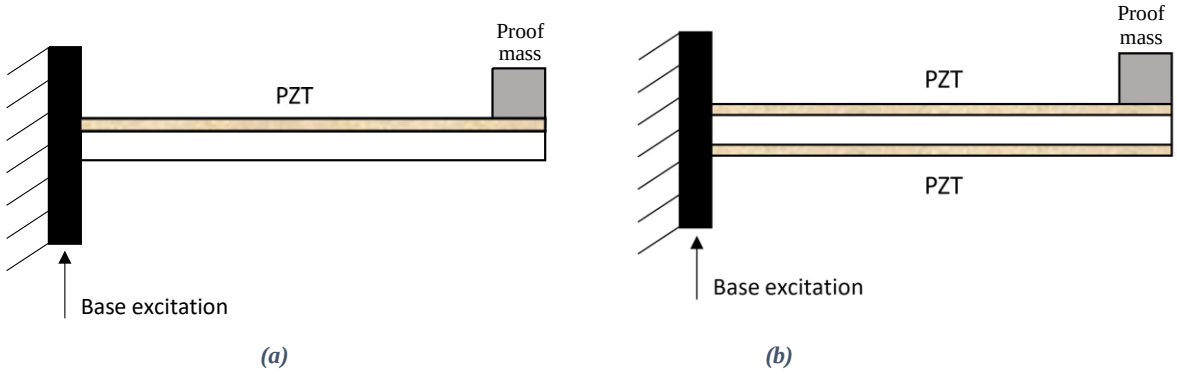

Figure 9. Unimorph straight cantilever (b) Bimorph straight cantilever

Fig. (9) shows the operation principle of a cantilever based PEH. As the structure where the cantilever is fixed vibrates, the cantilever to oscillate. These bending oscillations induce strains in the cantilever, the mechanical elastic energy that is induced in the piezoelectric elements is converted into electrical energy, since one side of the cantilever beam becomes under tension along its length, while the opposite side experiences compression along the same direction, opposite electrical charges relative to the polarization directions are generated. The non-piezoelectric shim sandwiched between both piezoelectric plates is employed in order to get better performance out of the cantilever. If the shim wasn't included, and the piezoelectric materials were in one piece, the electric charges would cancel each other out and there would be no energy harvested [6,45,48].

Baker et al. [30] found that loading a triangular beam results in higher strains compared to the trapezoidal harvesters while the rectangular harvester provides the least strain when subjected to the same loading. They performed experiments on rectangular and trapezoidal cantilever PEHs, they found that the trapezoidal PEH produced 30% more power (more strain), nothing that they are smaller in size. The harvesters were tested in the resonance mode and frequency matching was

performed as explained in section V, due to the high fatigue stresses subjected on the harvester in the resonance mode and the stress concentration points at the fixation points, a maximum strain of 1 m*strain* is recommended.

Many researchers have been experimenting the cantilever based PEHs. Table (5) demonstrates some of the current designs including the Unimorph [49],[50], bimorph [45,48,51,52] and tapered cantilever beam [49,53] PEHs.

Table 5. A comparison between different configurations of cantilever based PEHs [54]

Reference	**Description**	**Size (*mm*)**	**Frequency**	**Power output**	**Load Resistance**
Glynne et al. [49]	Tapered PZT unimorph cantilever with a proof mass	L = 10, W_{root} = 20, W_{tip} = 10, t = 0.07	80.1 *Hz*	2.1 µ*W*	333 *k*Ω
Roundy et al. [45,48]	Bimorph cantilever	1-cm^3 rectangular cantilever	120 *Hz*	375 µ*W*	300 *k*Ω
Wang et al. [52]	Air-spaced bimorph cantilever Fig. (7a)	L = 7, W = 7.4, t = 0.127	545 *Hz*	32 mV/g output voltage	NA
Challa et al. [55]	Piezoelectric cantilever beam with magnetic field applied at the free end Fig. (10 b)	L = 34, W = 20, t = 0.6	26.2 *Hz* (±20% tunable)	2.4 µ*W*	26 *k*Ω
Mehraeen et al. [53]	Tapered cantilever beam with proof mass	L = 150	47 *Hz*	5*mW*	NA
Gao et al. [50]	PZT unimorph cantilever with stainless steel (SS) layer	$L_{PZT} = L_{SS}$, W =5.5, t = 127	90 *Hz*	5.75 µ*W*	NA
Choi et al. [56]	MEMS bimorph structure with proof mass at the free end	L = 0.26, W = 0.17	13.97 *KHz*	1 µ*W*	5.2 *M*Ω

Cantilever based energy harvesters are widely used in aerospace applications to in powering wireless sensor networks, the source of excitation for this case is the air flow across a proof mass attached to the free end, the proof mass can be in the form of a an airfoil (flutter), cube, cuboid as shown in Fig. (10), cylinder, prism, etc. The fluid flow across the proof mass exits a lateral vibratory movement for the harvester, this is typically the case for vortex induced vibration (VIV) based and galloping based PEHs, for the wake galloping PEH an extra body is added upstream the proof mass that creates Karman vortex [57] that magnifies the movement of the proof mass and hence the power generated.

The harvested energy from the three harvesters types flutter [58,59], VIV [59,60], galloping [61–63] PEHs vary according to the flow *Reynold's number*, proof mass weight and dimensions as well as the piezoelectric material used and the number of layers which makes the comparison between the current designs' performance difficult, however, the VIV based PEHs is known to produce the least power while the galloping based PEHs are the simplest to design and efficient in flows with low Reynold's numbers.

Flextensional Piezoelectric Harvesters "PEH"

The first reported flextensional PEH was proposed by Kim et.al [64] in Penn State University, the flextensional harvesters are known to produce higher power compared to the other types of harvesters, in this subsection we focus on 3 types of flextensional energy harvesters namely the circular cymbal, 33 and circular diaphragm mode FEHs. The Flextensional harvesters are known to produce power outputs of at least 1 order of magnitude higher compared to other harvester types.

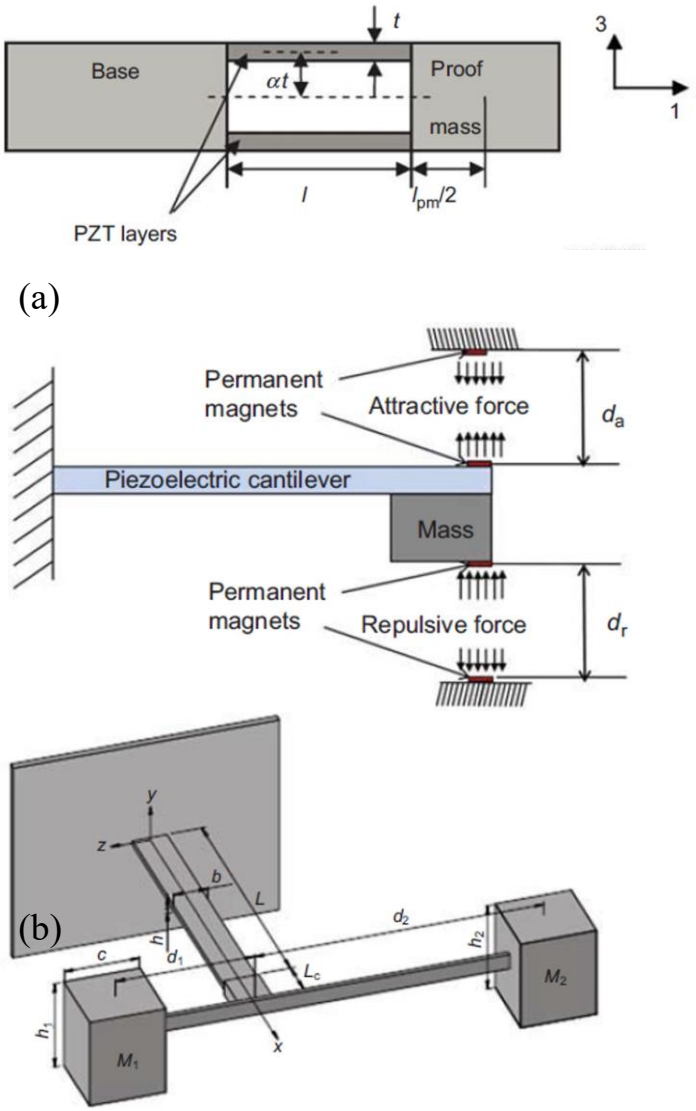

Figure 10. Diagrams of advanced cantilever PEHs. (a) Air-spaced cantilever PEH [52] (b) Magnetic field tuned cantilever PEH [55] and (c) Undergoing bending torsion vibration cantilever PEH [65]

Shabara [66] performed an investigation on the “33” mode Flextensional Piezoelectric Energy Harvesters (FPEH) in resonance and off-resonance modes. Four numerical models were used to, quasi-static model, single degree of freedom model (SDOF), A Distributed Parameter

Model and a Finite Element Model (FEM), the distributed parameter model was found to give the most accurate result with almost zero error, while the finite element model was found to give the highest error that reached 15.48%. The recommended model in his work was the quasi-static mode. The quasi-static model was the easiest to compliment and provided a relatively accurate result as shown in the table below.

Table 6. A Summary of off Resonance Mode Models Result

Model	$V_{max}(Volt)$	$V_{RMS}(Volt)$	$E_{RMS}\%$
Quasi-Static Model	5.824	4.1182	7.733%
SDOF Model	3.791	2.6806	25.1661%
ANSYS Model	6.243	4.4145	15.4542%
Analytical Model	5.406	3.8226	0.0%

Also, in the same work Shabara [66] provided insights on the resonance mode FEA simulations. It was reported that the resonance mode produces much higher voltage compared to the off-resonance mode. However, the higher stresses exerted on the force amplification frame near natural frequencies is extremely high that can lead to the failure of the frame if its poorly designed.

Shabara [66] also reported that the deviation in the resonance frequency between the ANSYS model and the experimental reading can be caused by the discrepancies between the designed and the manufactured harvester's frames because of the are extremely small dimensions of the harvester.

III. CONSTITUTIVE EQUATIONS

This chapter will cover the equations which define the electromechanical properties of piezoelectric materials. Our main source for these equations is the IEEE standard for piezoelectricity [22] which is widely accepted as being a reliable depiction of piezoelectric material properties. The main assumption in the IEEE standard is that piezoelectric materials behave linearly. This behavior is only found at low mechanical stress levels and low electric fields. However, at high electric fields and high mechanical stresses, piezoelectrics behave in a nonlinear way which will not be covered in this write up.

As described in the previous section, the direct piezoelectric effect is a when mechanical strain is applied to a piezoelectric material which causes it to become electrically polarized, producing a surface electric charge. This is the foundation upon which piezoelectrics are used as sensors. Furthermore, piezoelectrics can be used as energy harvesters by attaching electrodes to the surfaces to collect the power produced once the material is strained.

The constitutive equations representing the piezoelectric property assume that the total strain in the piezoelectric material is equal to the sum of the mechanical strain resulting from the applied mechanical stress in addition to the controllable actuation strain caused by an applied electric voltage through the material. The axes in the system are identified by numbers instead of letters; x, y, and z are represented as 1, 2, and 3 respectively [7]. The constitutive equations used to define a linear piezoelectric material are written as [22]:

$$\varepsilon_i = S_{ij}^E \sigma_j + d_{mi} E_m \tag{9}$$

$$D_m = d_{mi}\sigma_i + \xi_{ik}^{\sigma} E_k \tag{10}$$

or,

$$\varepsilon_i = S_{ij}^{D}\sigma_j + g_{mi}D_m \tag{11}$$

$$E_i = g_{mi}\sigma_i + \beta_{ik}^{\sigma} D_k \tag{12}$$

which is the more popular form used for applications that involve sensing.

Where the indices $i, j = 1, 2, \ldots, 6$ and m , $k = 1, 2, 3$ which refer to the different directions within the material coordinate system. Table 7 lists the different coefficients including their units. Furthermore, the superscripts $E, \sigma, and\ D$ signify that the measurement was taken at constant electric field, constant stress, and constant electrical displacement respectively. The physical meanings of these variables will be explained in the following section.

Table 7: List of coefficients and their units

Coefficient	Definition	Unit
σ	Stress vector	N/m^2
ε	Strain vector	m/m
E	vector of applied electric field	V/m
ξ	Permittivity	F/m
d	Piezoelectric charge constant matrix	m/V
S	Compliance matrix	m^2/N
D	Electric displacement matrix	C/m^2
g	Piezoelectric voltage constant matrix	m^2/C
β	Impermittivity component	m/F

Equations 12 and 15 represent the indirect piezoelectric effect (when the material is used as an actuator applied voltage gives displacement) and equations 3 and 5 represent the direct piezoelectric effect in the case that the material is used as a sensor. Equations 2-4 can be written in matrix form as:

$$\begin{bmatrix}\varepsilon_1\\ \varepsilon_2\\ \varepsilon_3\\ \varepsilon_4\\ \varepsilon_5\\ \varepsilon_6\end{bmatrix}=\begin{bmatrix}S_{11} & S_{12} & S_{13} & S_{14} & S_{15} & S_{16}\\ S_{12} & S_{22} & S_{23} & S_{24} & S_{25} & S_{26}\\ S_{13} & S_{23} & S_{33} & S_{34} & S_{35} & S_{36}\\ S_{14} & S_{24} & S_{34} & S_{44} & S_{45} & S_{46}\\ S_{15} & S_{25} & S_{35} & S_{45} & S_{55} & S_{56}\\ S_{16} & S_{26} & S_{36} & S_{46} & S_{56} & S_{66}\end{bmatrix}\begin{bmatrix}\sigma_1\\ \sigma_2\\ \sigma_3\\ \sigma_4\\ \sigma_5\\ \sigma_6\end{bmatrix}+\begin{bmatrix}d_{11} & d_{21} & d_{31}\\ d_{21} & d_{22} & d_{32}\\ d_{31} & d_{23} & d_{33}\\ d_{41} & d_{24} & d_{34}\\ d_{51} & d_{25} & d_{35}\\ d_{61} & d_{26} & d_{36}\end{bmatrix}\begin{bmatrix}E_1\\ E_2\\ E_3\end{bmatrix} \tag{13}$$

and

$$\begin{bmatrix}D_1\\ D_2\\ D_3\end{bmatrix}=\begin{bmatrix}d_{11} & d_{12} & d_{13} & d_{14} & d_{15} & d_{16}\\ d_{21} & d_{22} & d_{23} & d_{24} & d_{25} & d_{26}\\ d_{31} & d_{32} & d_{33} & d_{34} & d_{35} & d_{36}\end{bmatrix}\begin{bmatrix}\sigma_1\\ \sigma_2\\ \sigma_3\\ \sigma_4\\ \sigma_5\\ \sigma_6\end{bmatrix}+\begin{bmatrix}e_{11}^{\sigma} & e_{12}^{\sigma} & e_{13}^{\sigma}\\ e_{12}^{\sigma} & e_{22}^{\sigma} & e_{23}^{\sigma}\\ e_{13}^{\sigma} & e_{23}^{\sigma} & e_{33}^{\sigma}\end{bmatrix}\begin{bmatrix}E_1\\ E_2\\ E_3\end{bmatrix} \tag{14}$$

where the shear stresses are represented as

$$\sigma_4 = \sigma_{23}$$

$$\sigma_5 = \sigma_{13}$$

$$\sigma_6 = \sigma_{12}$$

Note that, from the above matrices, we can see that in general, there are 21 independent elastic constants, 18 independent piezoelectric constants, and 6 independent dielectric constants.

Since piezoelectric ceramics are considered to be transversely isotropic, and we assume that the poling direction is in the 3 direction, many of the parameters will become zero and others can be expressed in terms of other parameters. Hence, the compliance matrix non-zero elements are:

$$S_{11} = S_{22}$$

$$S_{13} = S_{31} = S_{23} = S_{32}$$

$$S_{12} = S_{21}$$

$$S_{44} = S_{55}$$

$$S_{66} = 2(S_{11} - S_{12})$$

For the piezoelectric strain constant matrix non-zero elements:

$$d_{31} = d_{32}\ and\ d_{15} = d_{24}$$

And for the dielectric coefficient matrix non-zero elements:

$$e_{11}^{\sigma} = e_{22}^{\sigma}\ and\ e_{33}^{\sigma}$$

Therefore, equations 5 and 6 can be simplified to:

$$\begin{bmatrix}\varepsilon_1\\ \varepsilon_2\\ \varepsilon_3\\ \varepsilon_4\\ \varepsilon_5\\ \varepsilon_6\end{bmatrix} = \begin{bmatrix} S_{11} & S_{12} & S_{13} & 0 & 0 & 0 \\ S_{12} & S_{11} & S_{13} & 0 & 0 & 0 \\ S_{13} & S_{13} & S_{33} & 0 & 0 & 0 \\ 0 & 0 & 0 & S_{44} & 0 & 0 \\ 0 & 0 & 0 & 0 & S_{44} & 0 \\ 0 & 0 & 0 & 0 & 0 & 2(S_{11} - S_{12}) \end{bmatrix} \begin{bmatrix}\sigma_1\\ \sigma_2\\ \sigma_3\\ \sigma_4\\ \sigma_5\\ \sigma_6\end{bmatrix} + \begin{bmatrix} 0 & 0 & d_{31} \\ 0 & 0 & d_{31} \\ 0 & 0 & d_{33} \\ 0 & d_{15} & 0 \\ d_{15} & 0 & 0 \\ 0 & 0 & 0 \end{bmatrix} \begin{bmatrix}E_1\\ E_2\\ E_3\end{bmatrix} \quad (15)$$

$$\begin{bmatrix} D_1 \\ D_2 \\ D_3 \end{bmatrix} = \begin{bmatrix} 0 & 0 & 0 & 0 & d_{15} & 0 \\ 0 & 0 & 0 & d_{15} & 0 & 0 \\ d_{31} & d_{31} & d_{33} & 0 & 0 & 0 \end{bmatrix} \begin{bmatrix} \sigma_1 \\ \sigma_2 \\ \sigma_3 \\ \sigma_4 \\ \sigma_5 \\ \sigma_6 \end{bmatrix} + \begin{bmatrix} e_{11}^{\sigma} & 0 & 0 \\ 0 & e_{11}^{\sigma} & 0 \\ 0 & 0 & e_{33}^{\sigma} \end{bmatrix} \begin{bmatrix} E_1 \\ E_2 \\ E_3 \end{bmatrix} \tag{16}$$

We can see that the number of independent constants has been greatly reduced due to the material being transversely isotropic. The number of independent elastic constants went down from 21 to 5, the number of independent piezoelectric constants went down from 18 to 3, and the number of independent dielectric constants went down from 6 to 3.

MECHANICAL CONSIDERATIONS

In the infinitesimal mechanical displacement of a piezoelectric material, the Cartesian components are denoted by u_i. The symmetric portion of the mechanical displacement is what determines the strain tensor S_{ij}. Hence,

$$S_{ij} = \frac{1}{2}\left(u_{i,j} + u_{j,i}\right) \tag{17}$$

where

$$u_{j,i} = \partial u_i / \partial x_j \tag{18}$$

The asymmetric portion of the mechanical displacement gradient is responsible for the infinitesimal local rigid rotation, which is of no consequence to the IEEE standard and is allowed to take place without constraint in the continuum [22]. The velocity of a point in the material is given by

$$v_i = \dot{u}_i = \partial u_i / \partial \mathrm{t} \tag{19}$$

where *t* is the time. The density of the material ρ will be constant for any material in this write up which is in agreement with the IEEE standard [22].

When there is a mechanical interaction between two portions of the continuum, which are separated by an arbitrary surface *S*, a traction vector is assumed to exist. This traction vector t_j^n is defined as the force per unit area acting on a surface at a point and depends on the unit normal n_i to the surface S. Based on the conservation of linear momentum, there exists a stress tensor σ_{ij}, which relates to the traction vector t_j^n by

$$t_j^n = \sigma_{ij} n_i \tag{20}$$

Using Cauchy's First Law of Motion,

$$\rho \frac{D v_i}{D t} = \frac{\partial \sigma_{ji}}{\partial x_j} + \rho f_i \tag{21}$$

And assuming that there are no body forces, we get the stress equations of motion as:

$$\frac{\partial \sigma_{ji}}{\partial x_j} = \rho \frac{D v_i}{D t} \tag{22}$$

where, σ_{ij} is symmetric due to the conservation of angular momentum.

ELECTRICAL CONSIDERATIONS

According to the IEEE standard, full electromagnetic equations are not usually needed. Since the phase velocities of acoustic waves are roughly five orders of magnitude less than the electromagnetic wave velocities, the quasi-electrostatic approximation is suitable.

Under these circumstances, electrical effects outweigh the magnetic effects rendering them insignificant. In electrical theory, the Cartesian components of the electric displacement and electric field are specified, respectively, by D_i and E_i. In metric units these two components are related by [22].

$$D_i = \xi_0 E_i + P_i \tag{23}$$

where P_i indicates the polarization vector components, and ξ_0 is the permittivity of free space which is equal to

$$\xi_0 = 8.854 \times 10^{-12}\ F/m \tag{24}$$

The electric field vector E_i which comes from the scalar electric potential:

$$E_i = -\varphi, i \tag{25}$$

The electric displacement vector D_i which satisfies the electrostatic equation for an insulator

$$D_{i,i} = 0 \tag{26}$$

IV. NUMERICAL ANALYSIS

Since analytical methods become extremely complex very quickly, we opted to use ANSYS workbench to simulate the piezoelectric energy harvester. ANSYS offers two methods for users to simulate their models: ANSYS workbench and ANSYS APDL. Each one has its own benefits.

ANSYS workbench has a very intuitive interface; users input the parameters of their model into the software and select which options they need. In addition, most of the materials used are readily available to the user and can just be selected. They can also add extensions for certain systems such as the Piezoelectric and MEMS ACT which we used to simulate our models. Furthermore, it interacts easy with other CAD packages, it allows for coupled analysis, geometry creation is simple using Space Claim and Design Modeler and has very advanced mesh controls.

On the other hand, APDL allows for more control over the model since each step of the problem must be specified by the user thus making the user aware of everything happening in the software. Additionally, it has a lower possibility of error, allows for more complex problems such as cases where a material behaves in a very particular way or the system has difficult equations to solve for. It also uses less computing memory since it does not have a complex GUI (Graphical User Interface). Finally, APDL's arguably most important feature is being able to codify a problem which allows for multiple runs for a simulation while changing parameters automatically (such as force or material).

PHYSICAL SETUP

To create the model correctly, we must first define our system and analyze the boundary conditions and external forces. The harvester's dimensions and material properties are show in Fig. 12 and Table 10. To simplify some of our work, we assumed that we have a Ford F150 (Fig. 13) pickup truck. This truck will be simulated in 3 different payloads:

1- No payload

2- Half the max payload

3- Max payload

This is to analyze the effect of the weight of the vehicle on the produced power. Additionally, the truck will also be simulated with 3 different speeds:

Table 8. Contact duration and time difference between front and rear wheel contact and various speeds

$\boldsymbol{Speed\ \left(\frac{mi}{hr}\right)}$	$\boldsymbol{Contact\ duration\ (s)}$	$\boldsymbol{Time\ between\ front\ and\ rear\ wheels\ (s)}$
25	0.0135	0.3224
45	0.0075	0.1791
60	0.0056	0.1343

To calculate the contact duration (t_d), we divide the length of the harvester by the speed of the vehicle as shown below.

$$t_d = \frac{150\ (mm)}{25\ \left(\frac{mi}{hr}\right) * \frac{1601000\left(\frac{mm}{mi}\right)}{3600\left(\frac{s}{hr}\right)}} = 0.0135\ s \tag{27}$$

Simulating the speed will help us study the effect of the duration of the force on the harvester and relate it to the generated power.

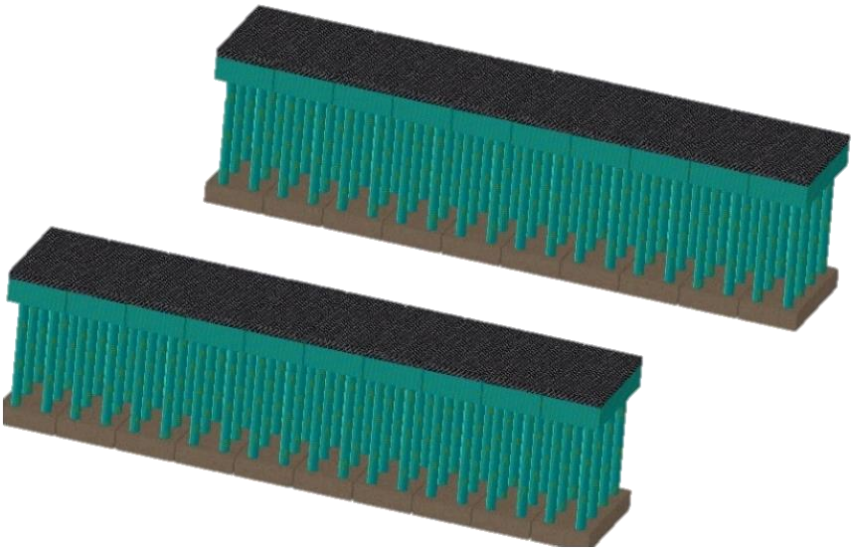

Figure 11. Diagram of ultra-high-power density roadway piezoelectric energy harvesting system

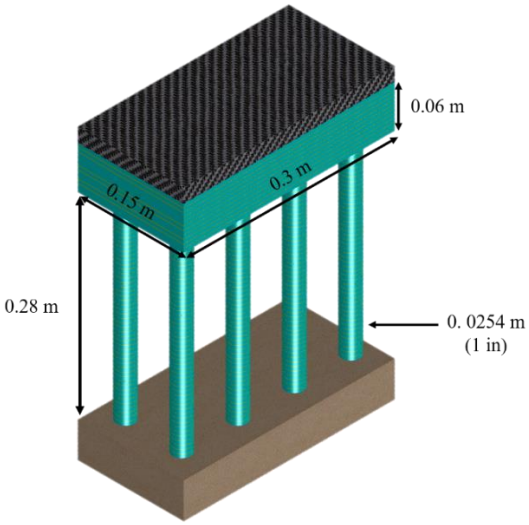

Figure 12. Dimensions of ultra-high-power density roadway piezoelectric energy harvesting system

Table 9. Physical and Piezoelectric properties of APC 855 [67]

$\boldsymbol{Relative\ Dielectric\ Constant\ (K^T)}$			3300
$Piezoelectric\ Voltage\ Constant\ (10^{-3}\ m^2/C)$			
$\boldsymbol{g_{33}}$	$\boldsymbol{-g_{31}}$	$\boldsymbol{g_{15}}$	
21	9	27	
$Young's\ Modulus(10^{10}\ N/m^2)$			
$\boldsymbol{Y_{11}^{\varepsilon}}$	$\boldsymbol{Y_{33}^{\varepsilon}}$		
5.9	5.1		
$\boldsymbol{Density\ (g/cm^3)}$			7.6

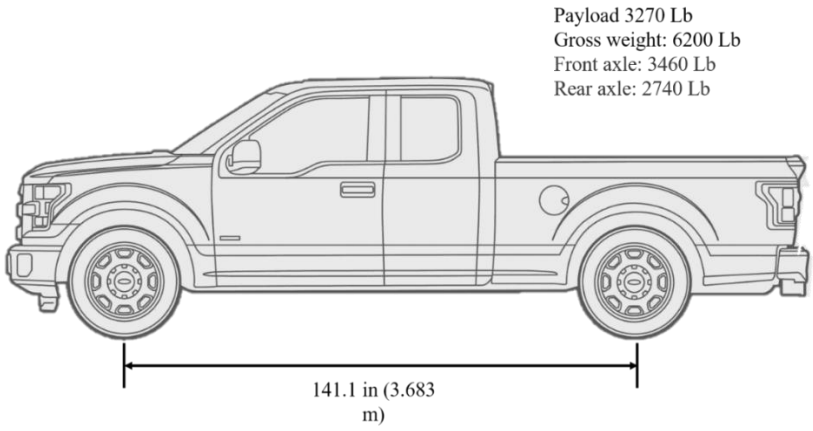

Figure 13. Ford F150 specifications

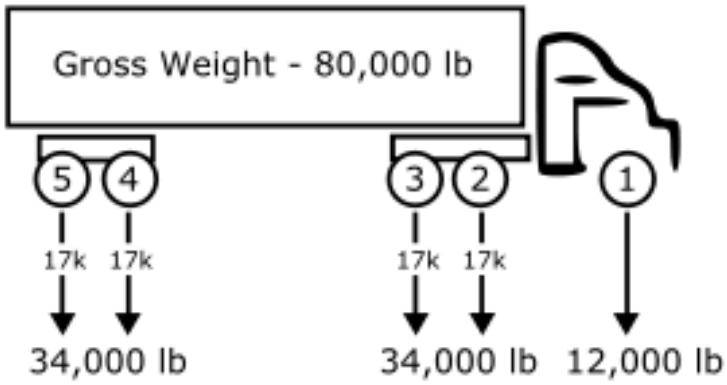

Figure 14. Full freight truck weight distribution

The free body diagram below illustrates the forces affected; once the car tire passes over the harvester, it induces two forces, a compressive force caused by the weight of the vehicle, and a shear force caused by the friction between the tire and the harvester's top surface.

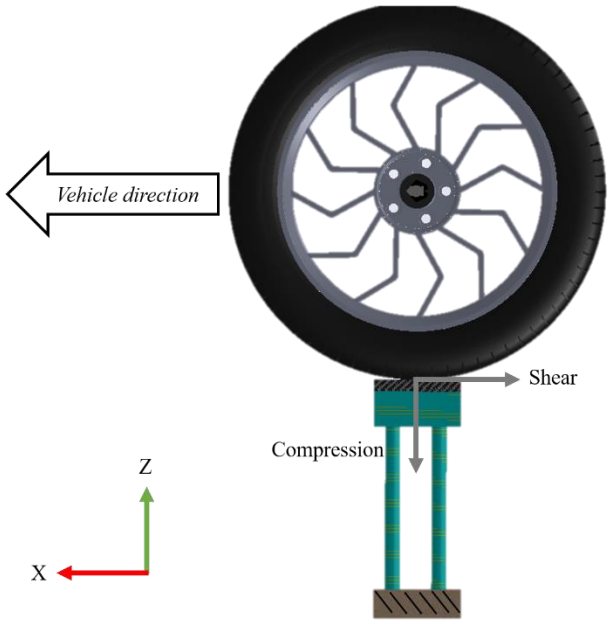

Figure 15. Free body diagram of the harvester

The compressive force F_c on a single harvester is calculated as:

$$F_c = \frac{3460\ (lb)}{2 * 2.204\left(\frac{lb}{kg}\right)} * 9.81\left(\frac{m}{s^2}\right) = 7{,}700\ N \tag{28}$$

Note that we divide by two since the front axle weight is distributed on two wheels.

To calculate the shear force F_s, we will assume that the road is dry, and the tires are new which gives a coefficient of friction μ of 0.7 [68]. We then multiply it by the normal force

$$F_s = \mu * n = 0.7 * \frac{3460\ (lb)}{2 * 2.204\left(\frac{lb}{kg}\right)} * 9.81\left(\frac{m}{s^2}\right) = 5{,}390\ N \tag{29}$$

Since the car's tire and the top surface of the harvester come into contact at a relatively high speed, the force is assumed to reach the maximum value instantly. After the tire passes over the harvester, the applied force cuts off right away and leaves the harvester to oscillate until it returns to its steady state. This occurs once for the front tires and a second time for the rear tires. Hence, the force on the harvester can be approximated as a square wave input as shown in fig 16 below.

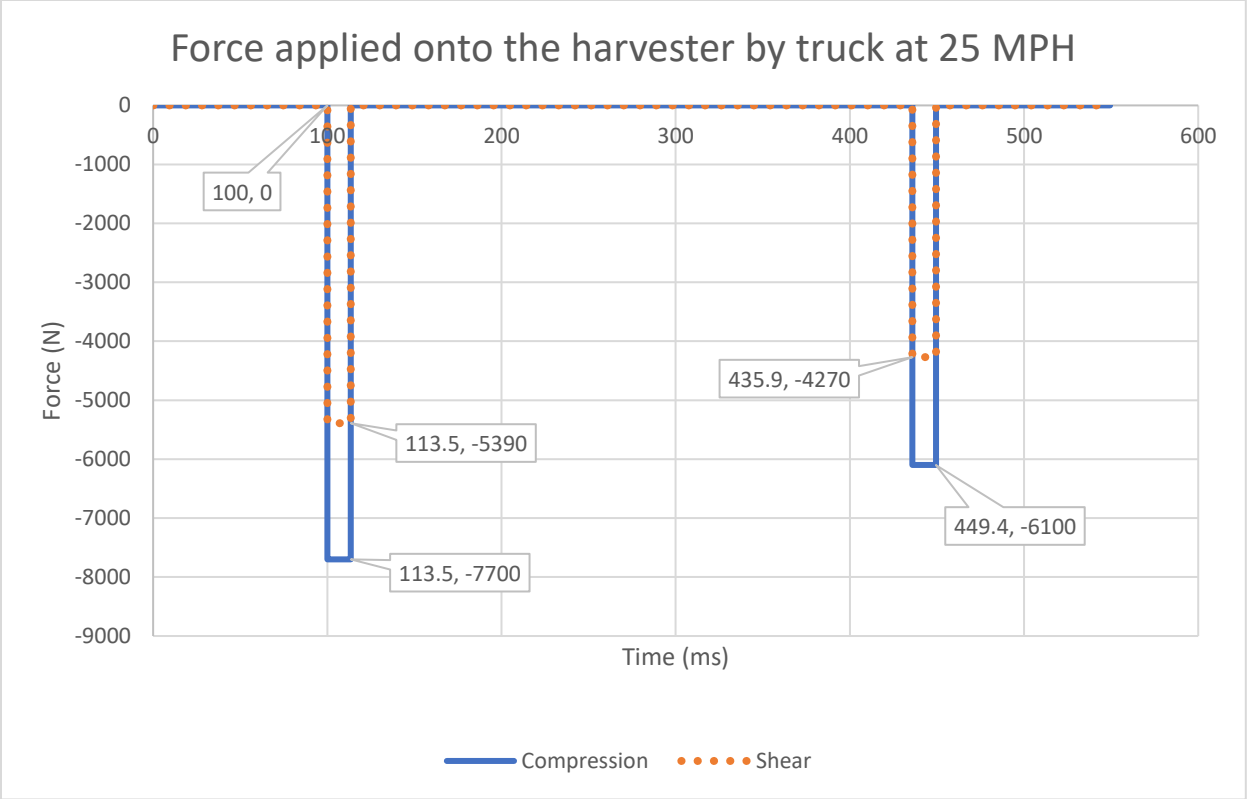

Figure 16. Force applied onto the harvester by the truck at 25 MPH

However, to properly assume that the force applied to the harvester instantaneously reaches the maximum, we must calculate the tire's contact patch (l_{cp}). This can be performed by dividing the single wheel load by the tire inflation pressure which is 35 psi [69] then multiplying by the tire width as shown below in fig 17

Figure 17. Contact patch [70]

$$l_{cp} = \frac{2740(lb)}{35(lb/in^2)} * 9(in) * 25.4\ \left(\frac{mm}{in}\right) = 220.93\ mm \quad (30)$$

Since 220.93 mm > 150 mm (width of the harvester), our assumption is correct.

SIMULATION SETUP

Two ANSYS models were used; static and transient. The static model was used mainly to ensure that all the boundary conditions and simulation setup was correct. The transient model contained most of the simulations since it is more realistic and accurate compared to an experiment.

The piezoelectric stack was modeled using ANSYS workbench mechanical and Mechanical APDL. First, the stack was drawn using Space Claim. To ensure accuracy and streamline the simulation, all separate layers were modelled and bonded together instead of assuming the stack to be a single block. This makes the voltage coupling of layers very easy and applicable through the workbench GUI instead of having to resort to APDL. Furthermore, it allows the user to plot results and contours on specific layers easily. After that, the model was assigned PZT material properties as in Table 9 and the mesh was generated. A fixed boundary condition was used at the bottom of the harvester to hold it in place. Also, a voltage reference boundary condition was assigned to the bottom surface of the top block and the top surface of the cylindrical block. After that, voltage couplings were applied between each layer. Finally, the force was applied to the top surface of the harvester and an open circuit simulation was ran with not damping. Note: We are only using $1/8^{th}$ of the model in the simulation to reduce the analysis time significantly. This also means that we need to apply a symmetry boundary condition at the sides of the model and force applied will be $1/8^{th}$ of the total force too.

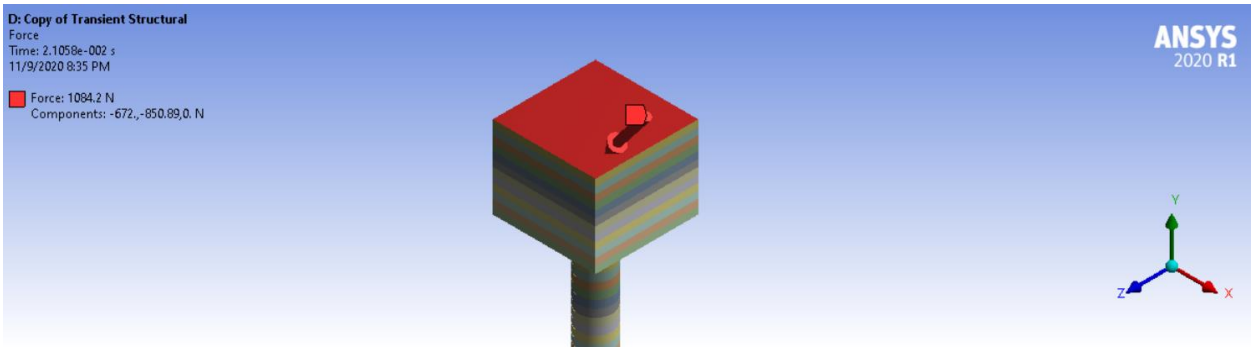

Figure 18. Force applied to the top surface of the harvester

Even though piezoelectric materials are anisotropic, the fact that the multilayers of the stack are very thin (as small as 5 mm) and the force is applied in the "33" direction for the bottom column and "15" mode for the top column, the piezoelectric effects in the other directions can be neglected. Hence, to simplify the model, we can assume that the piezoelectric stack is isotropic.

In order to treat the piezoelectric multi-layer stack as a single layer bulk piezoelectric block, we must apply the equivalence method used by Qian et al. [71]. This method assumes that:

$$\overline{C_P} = C_P \tag{31}$$

where $\overline{C_P}$ is the capacitance of the piezoelectric bulk and C_P is the capacitance of the multi-layer stack.

To calculate the capacitance of the piezoelectric bulk we use the following equation

$$\overline{C_P} = \frac{\varepsilon_{33}^{\sigma} A}{L} \tag{32}$$

where $L = pt_p$, and the expression for the multi-layer stack is:

$$C_P = \frac{p\varepsilon_{33}^{\sigma} A}{t_p} \tag{33}$$

Hence, by using Eqs. (30), (31), and (32), we get

$$\frac{\varepsilon_{33}^{\sigma} A}{p t_p} = \frac{p\varepsilon_{33}^{\sigma} A}{t_p} \tag{34}$$

Accordingly, the equivalent dielectric constant can be expressed as

$$\varepsilon_{33}^{\sigma} = p^2 \varepsilon_{33}^{\sigma} \tag{35}$$

ANSYS models were simulated under various conditions to determine the optimal conditions that the energy harvester should be operating at. The following assumptions were made:

1- The harvester is subjected to compression and shear when it meets the vehicle's tires.
2- The force that the vehicle applies to the harvester is 1/8th of the car's total mass and was approximated as 1 quarter of a sine wave since the force increases suddenly when the car runs over it and cuts off once the car passes it.
3- All piezoelectric layers are polarized in the same direction

In ANSYS, the piezoelectric matrix differs from the matrix used in the IEEE standard as shown below:

$$e_{ij}^{APDL} = \begin{bmatrix} e_{11} & e_{12} & e_{13} \\ e_{21} & e_{22} & e_{23} \\ e_{31} & e_{32} & e_{33} \\ e_{61} & e_{62} & e_{63} \\ e_{41} & e_{42} & e_{43} \\ e_{51} & e_{52} & e_{53} \end{bmatrix}$$

whereas the IEEE defines it as

$$e_{ij}^{IEEE} = \begin{bmatrix} e_{11} & e_{12} & e_{13} \\ e_{21} & e_{22} & e_{23} \\ e_{31} & e_{32} & e_{33} \\ e_{41} & e_{42} & e_{43} \\ e_{51} & e_{52} & e_{53} \\ e_{61} & e_{62} & e_{63} \end{bmatrix}$$

In addition, for transient analysis, a sparse solver is used instead of the default iterative solver. This is performed using EQSLV, SPARSE. Additionally, it is important to note that the sparse solve is only applicably to ANSYS full methods and not reduced or superposition methods.

Closed circuit simulation

To develop the closed circuit simulation, we follow the exact same steps as the open circuit simulation in ANSYS workbench except for 2 voltage couplings at the bottom and top surface of the harvester and the voltage reference we added initially are disabled. These parameters will be added through APDL since we need to assign a new CIRCU94 element which allows us to add a resistance to the system. The code in the appendix explains how to create the resistances.

The resistance applied between each material is found by calculating the capacitance of the harvester

$$\overline{C_P} = \frac{\varepsilon_{33}^{\sigma}\varepsilon_0 A}{L} = \frac{8 * 3300 * 8.854 \times 10^{-12} * (25.4 \times 10^{-3})^2 * \pi}{50 * 4 * 5.6 \times 10^{-3}} = 423\ nF \qquad (36)$$

Then using the following equation to calculate the impedance in ohms

$$Z_P = \frac{1}{2\omega C_P} \qquad (37)$$

where ω is the natural frequency of the system found by performing a modal analysis. Substituting gives:

$$Z_{P_{Bottom}} = \frac{1}{2\omega C_P} = \frac{1}{2*30.35*423\times10^{-12}} = 3.8947 \times 10^7\ \Omega, \quad (38)$$

$$Z_{P_{TOP}} = 7.5179 \times 10^5\ \Omega$$

Note that the impedance value is very large which indicates that the internal resistance is large.

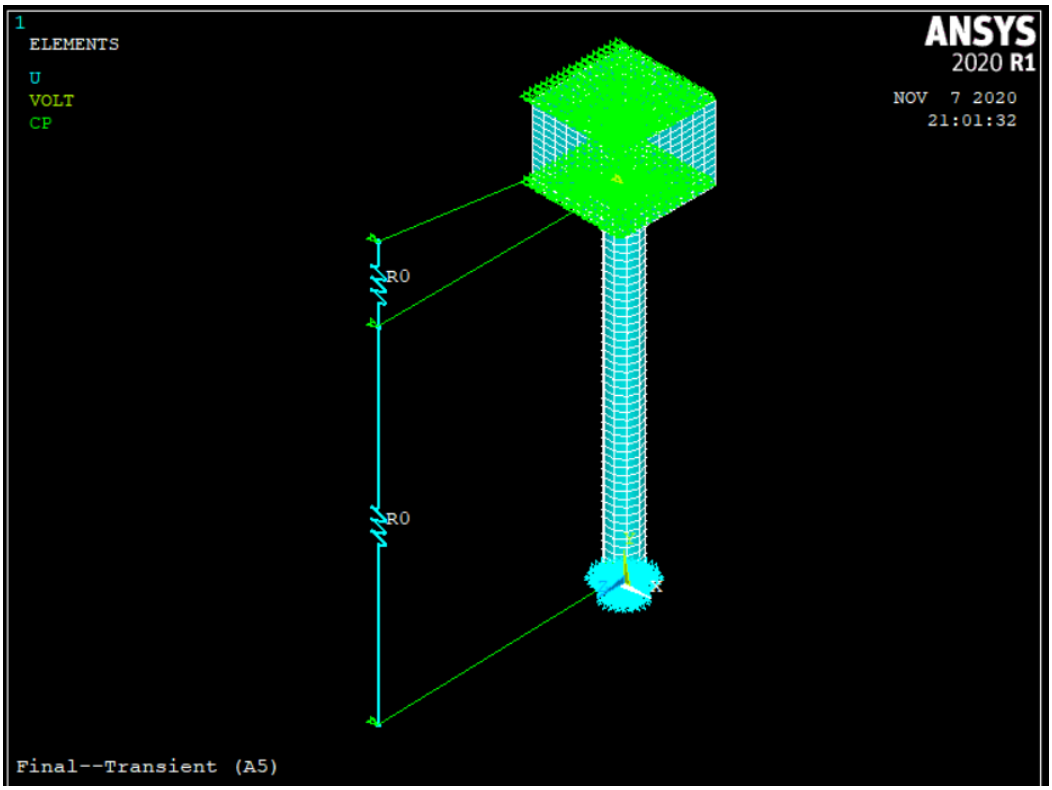

Figure 19. APDL Model displaying the resistances connected to the harvester

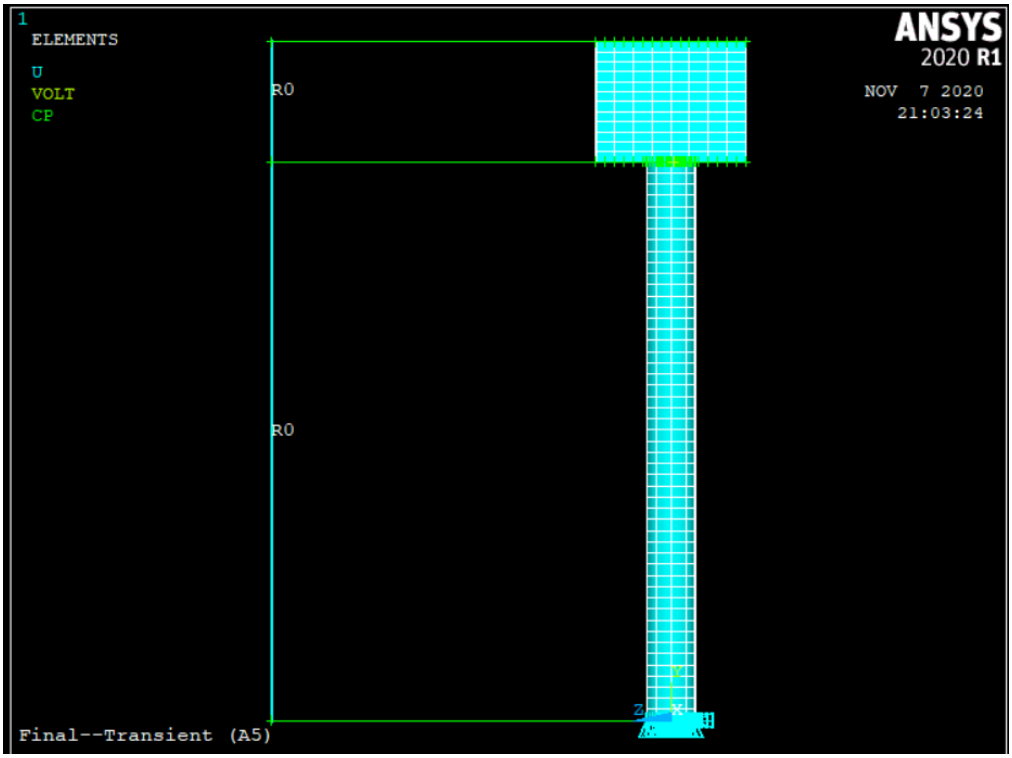

Figure 20. Side view of the APDL Model

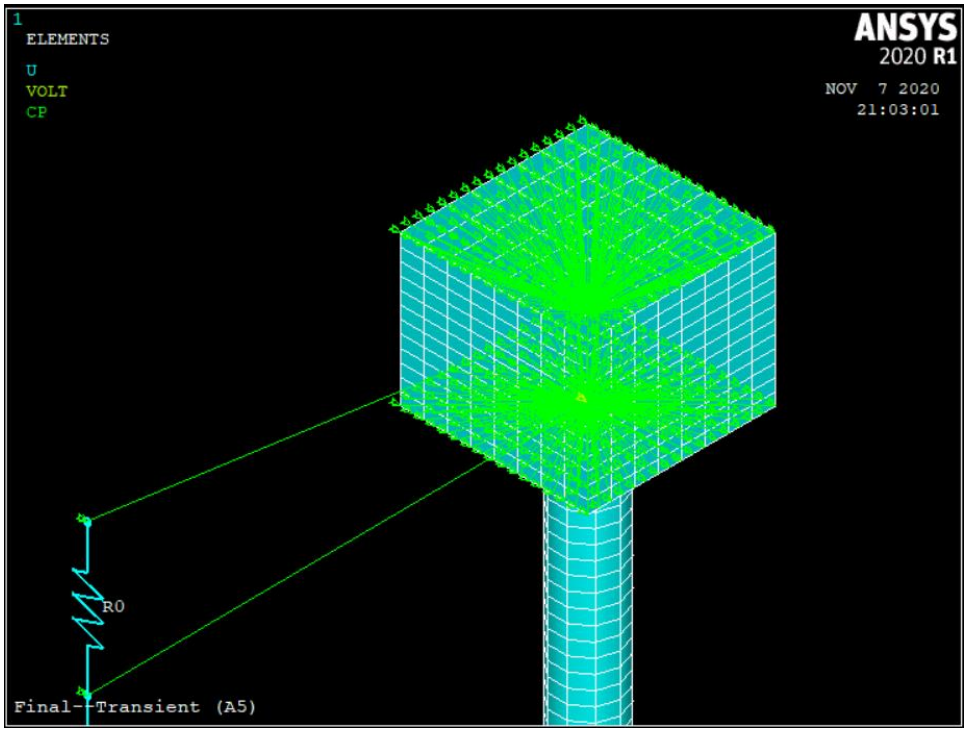

Figure 21. Coupling of CIRCU94 with layer nodes.

To calculate the total power output of a freight truck passing over the harvester

$$P = \frac{V^2}{R} \tag{39}$$

$$P_{RMS} = \sqrt{\frac{1}{n}\sum_i P_i^2} = 1.2908\,W, \tag{40}$$

$$P_{Total} = 2 * 1.2908 = 2.5816\,W \tag{41}$$

$$E = P_{RMS} * t = 2.5816 * 0.714 = 1.843\,J \tag{42}$$

For 10 blocks in a row connected in parallel

$$E_{10} = 1.843 * 10 = 18.43\,J \tag{43}$$

Suppose 300 trucks/hr

$$E_{hourly} = 18.43 * 300 = 5530\,\frac{J}{hr} \tag{44}$$

V. RESULTS AND DISCUSSION

MODAL ANALYSIS

Modal analysis was performed to in order to define the mode shapes and frequencies that were used to simulate our model. This was especially useful when performing impedance matching for our system as shown in Eq. 40. As we can see in Fig. 22 and Fig. 23, the main two mode shapes that affected our model were the bending and compressive modes at 30.349 Hz and 865.36 Hz respectively. However, since the compressive mode had a very high frequency, it decayed much quicker which left the bending mode to be the most dominant and generate the highest power. Hence, the bending mode's frequency value was used in our calculations.

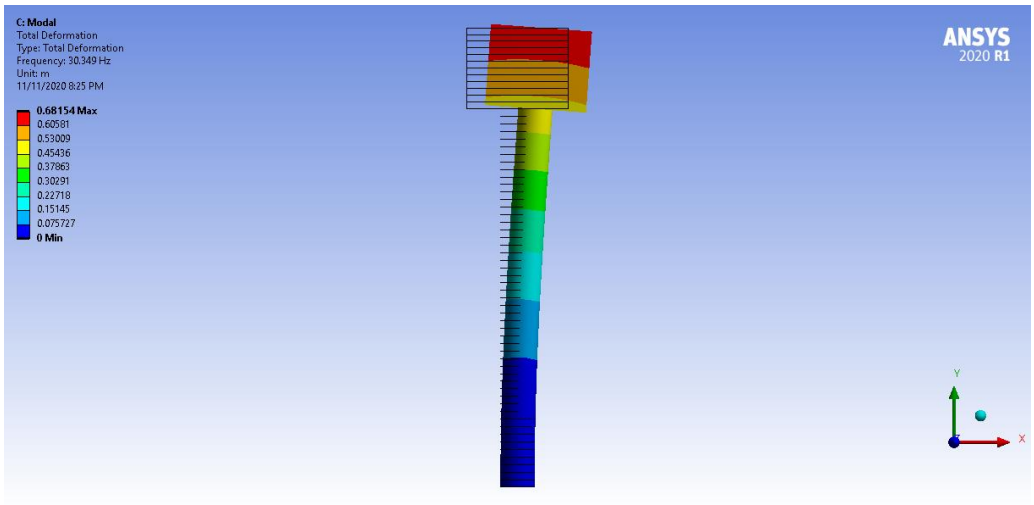

Figure 22. Bending Mode Shape @30.349 Hz

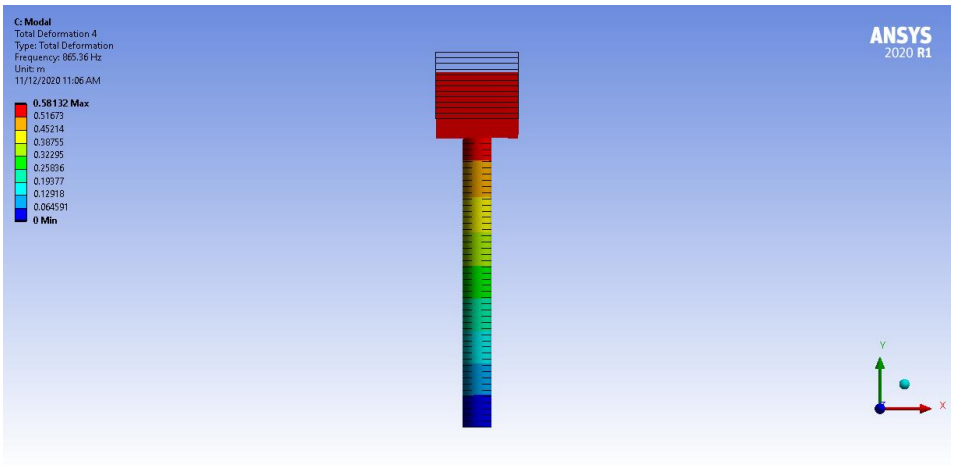

Figure 23. Compression Mode Shape @865.36 Hz

Simulations with coarse, medium, and fine mesh sizes were run in order to ensure that the number of elements didn't affect the results of the analysis. Since the coarse mesh did not vary much from the medium and fine meshes as seen in fig. 24, and the simulation time was 1/5th the fine mesh, it was used for all simulations.

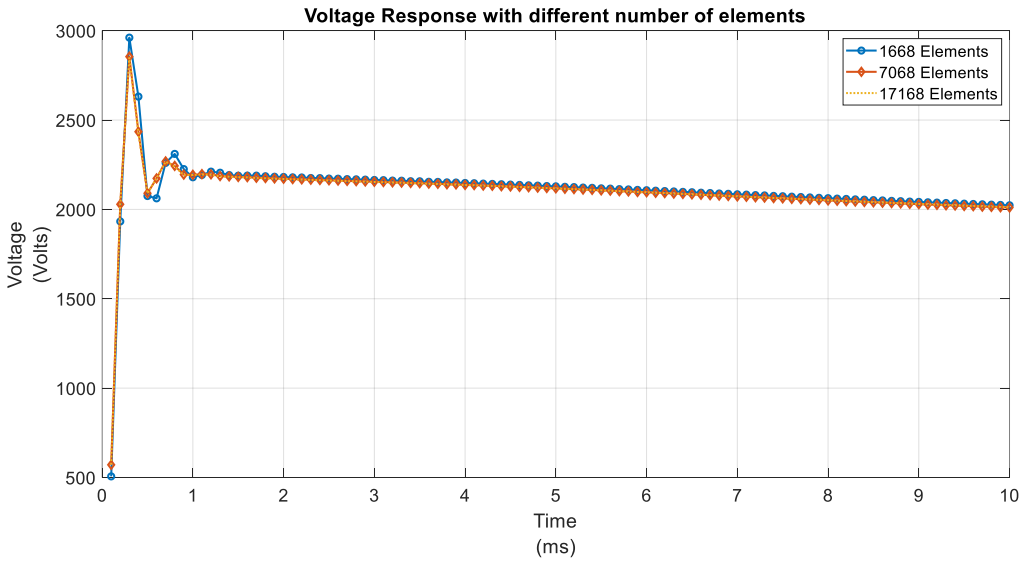

Figure 24. Voltage output comparison between various number of elements vs. time

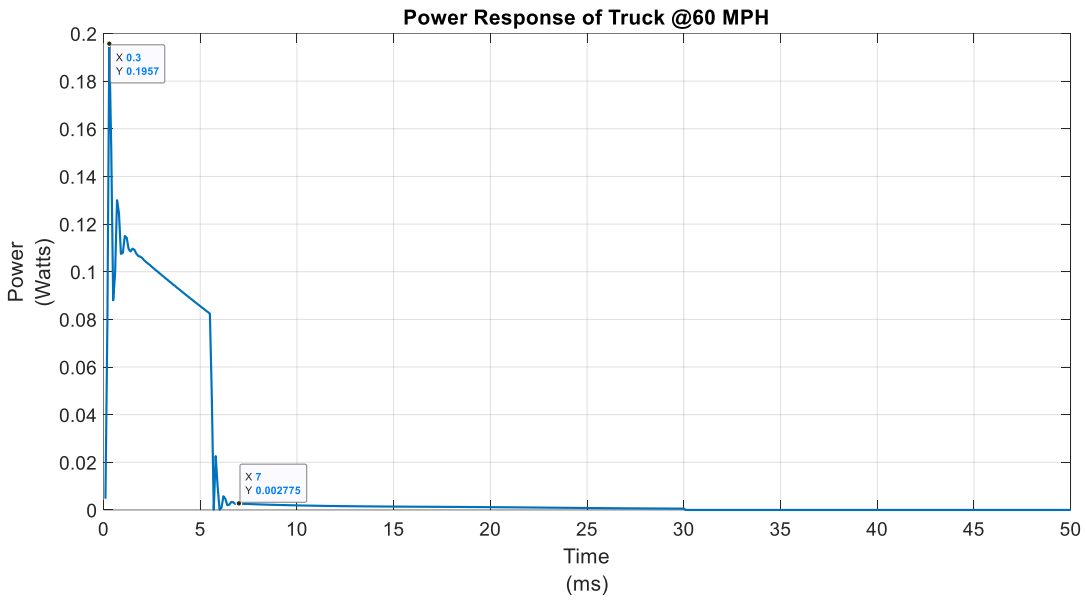

Figure 25. Instantaneous power output vs. time of truck at 60 MPH

VEHICLE SPEED

A comparison between the vehicle's speed and the power output was performed. As epicted in fig. 26 he slower the vehicle, the more power that will be generated since stress is induced over a longer duration.

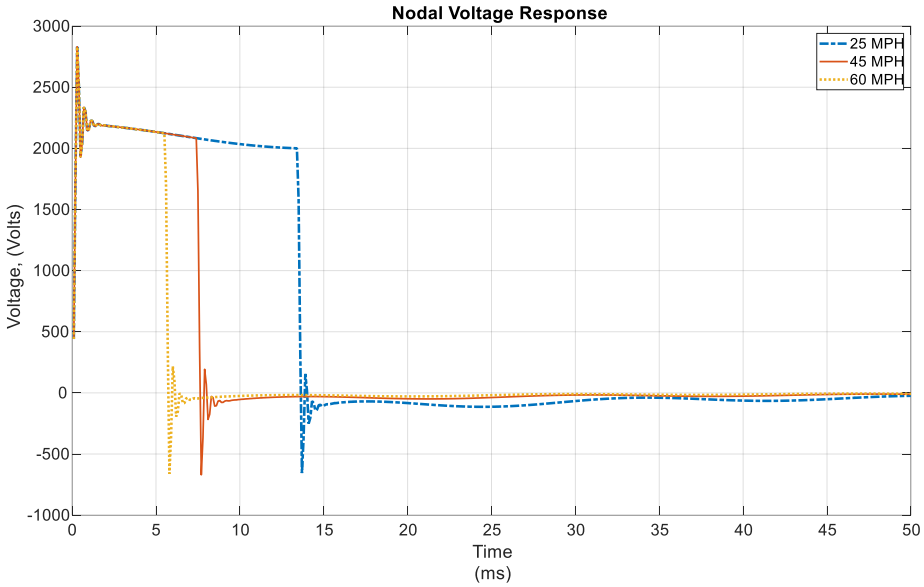

Figure 26. Comparison between vehicle speed and voltage output vs. time.

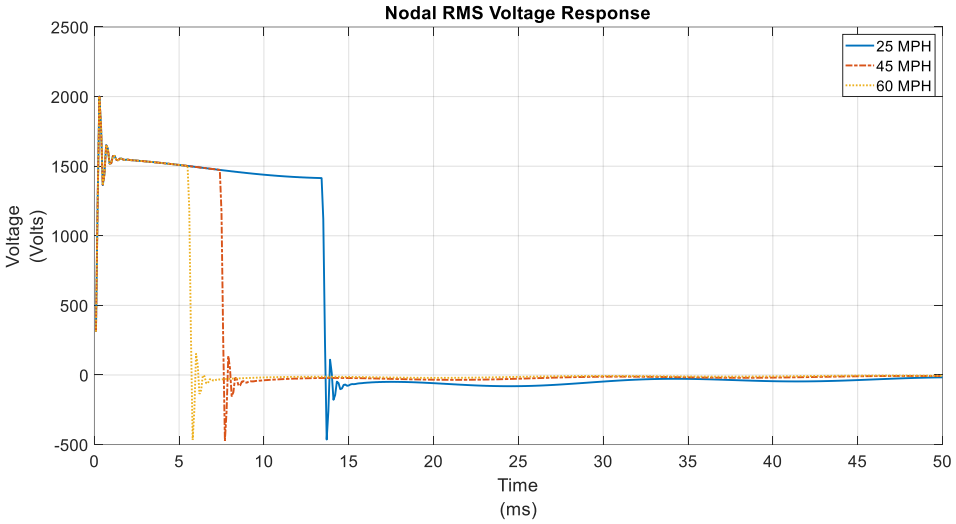

Figure 27. RMS value of voltage output at various vehicle speeds vs. time

Fig 27 displays the voltage output response from a vehicle passing over the harvester. It can be observed that there was a voltage difference of around 500 V since the load on the rear axle is lower than the load on the front axle.

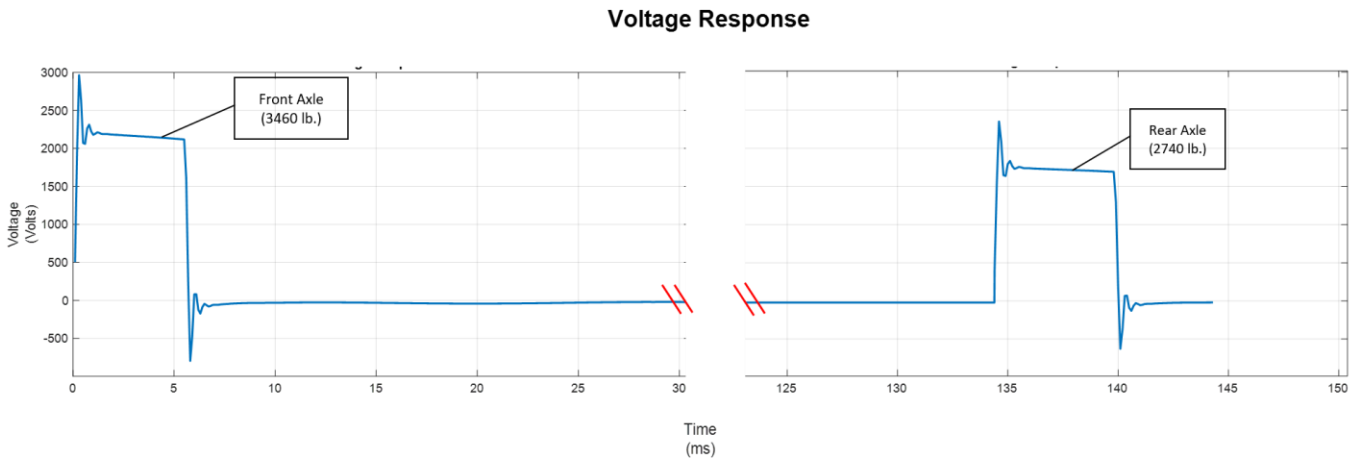

Figure 28. Voltage Output from a vehicle passing over the harvester @60MPH vs. time

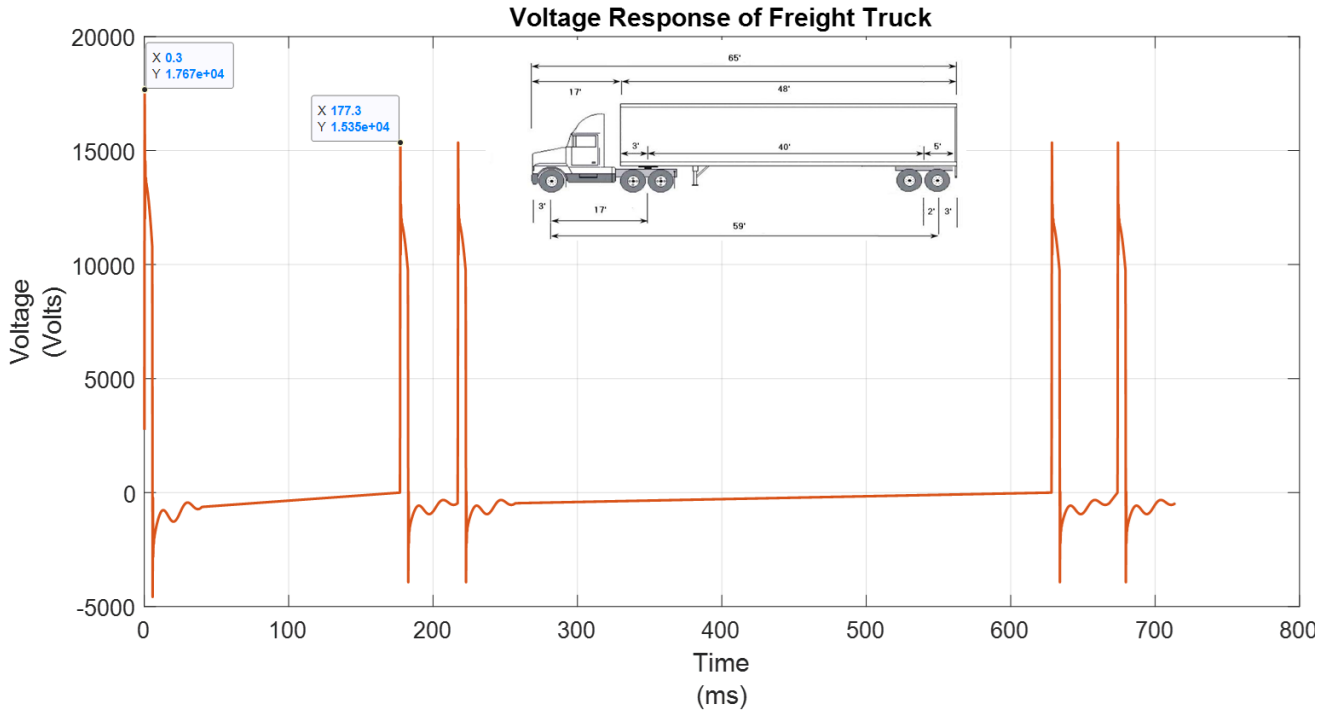

Figure 29. Voltage output from freight truck passing over the harvester at 60 MPH vs. time

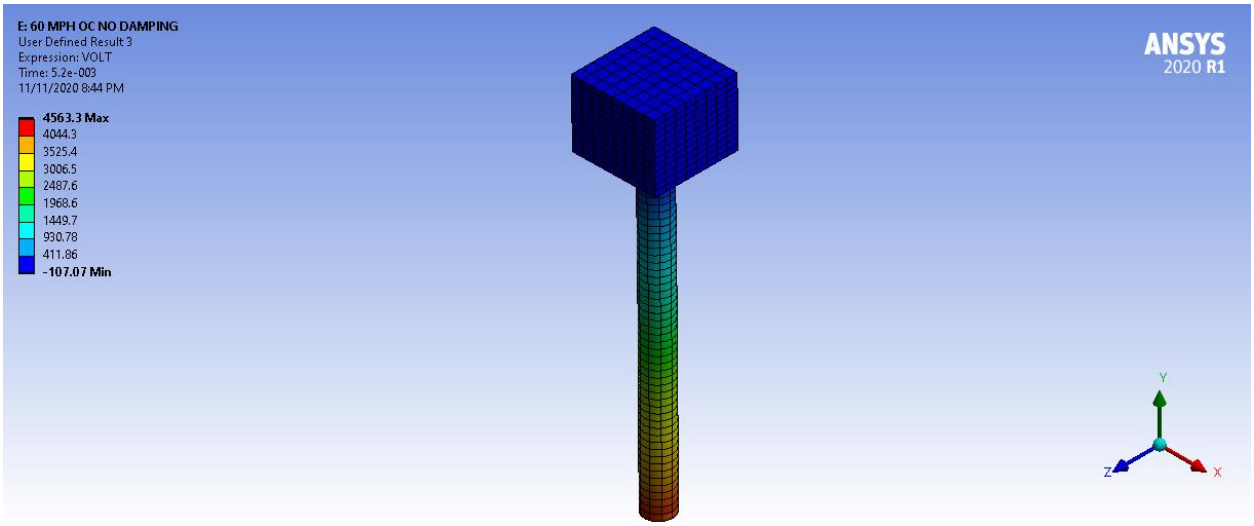

Figure 30. Contour plot of voltage for the harvester.

To ensure that our harvester does not fail when a vehicle passes above it, a stress analysis was performed as depicted in fig. 31. However, since the maximum stress is 75.1 MPa and the tensile strength of APC 855 is 28 MPa [72] failure will occur in the harvester. By applying a frictionless support to approximate the harvester being placed in the ground with dirt around it as seen in fig. 32, the stress drops down to 2.45 MPa which gives a factor of safety of ~12 which is illustrated in fig. 31. Also, if we analyze the voltage output between both models as in fig. 28 and 29, the maximum voltage drops from 3150 to 2220 V.

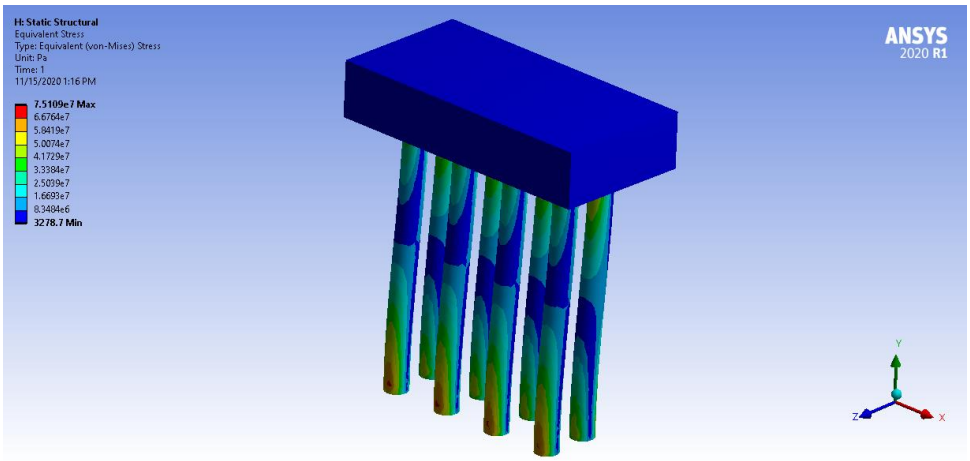

Figure 31. Stress contour plot for the harvester without supports.

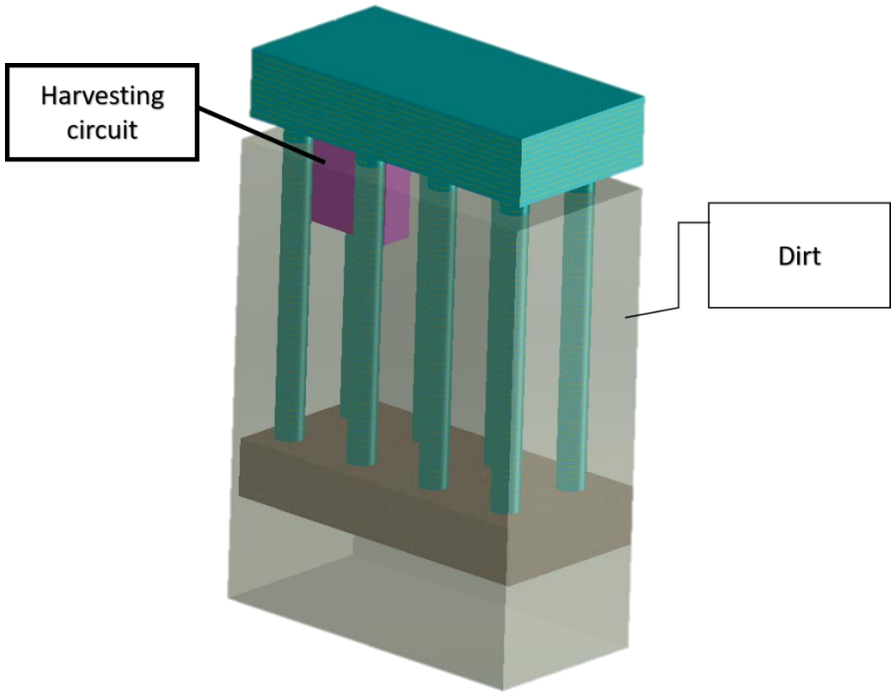

Figure 32. Energy harvester placed inside the ground.

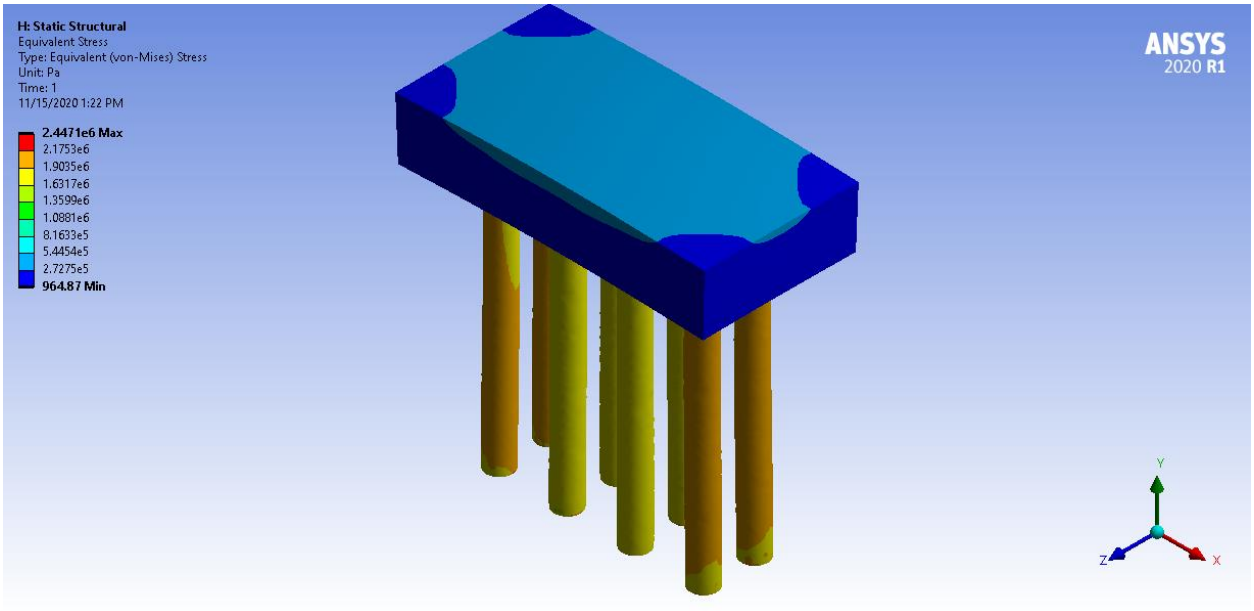

Figure 33. Stress contour plot for the harvester with frictionless supports.

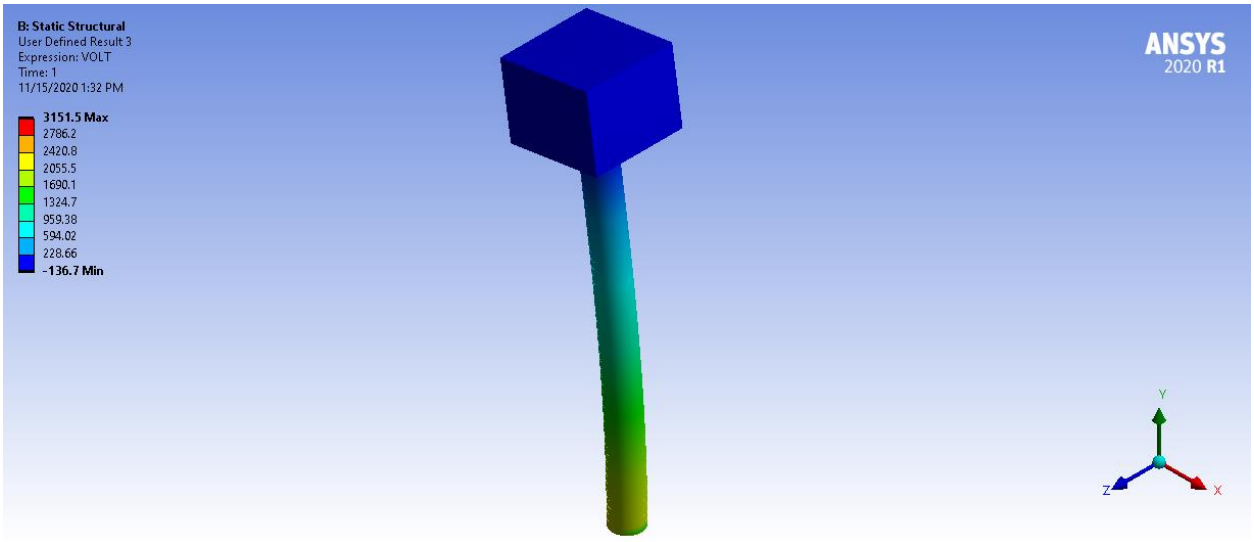

Figure 34. Voltage contour plot without support.

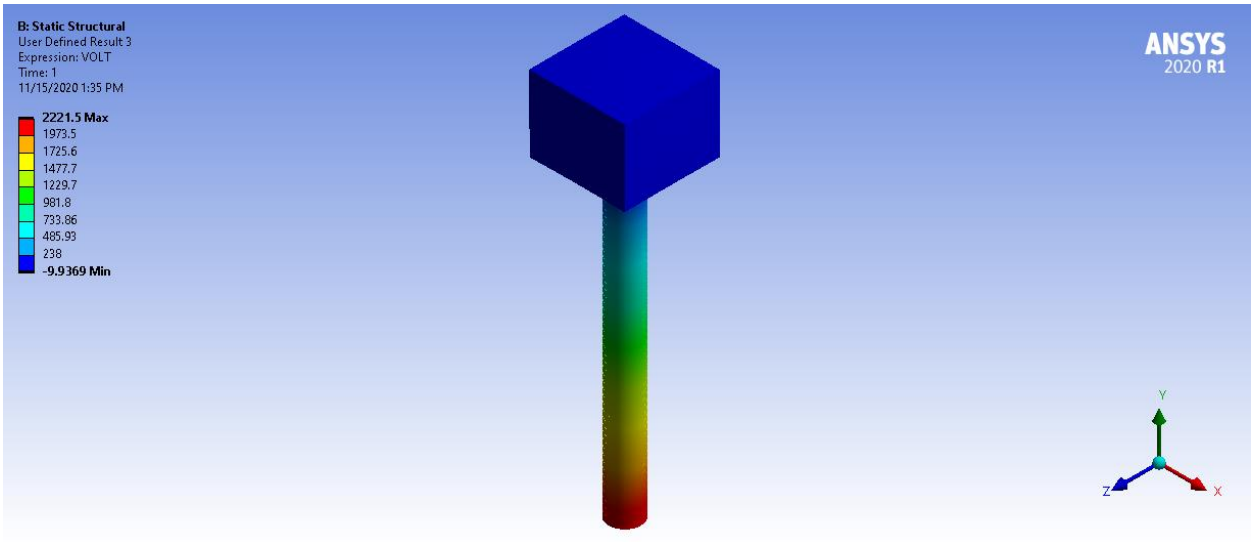

Figure 35. Voltage contour plot with frictionless support.

STIFFNESS COEFFICIENT (RAYLEIGH DAMPING)

Rayleigh damping is viscous damping that is proportional to a linear combination of stiffness and mass. The damping matrix C is given by

$$C = \mu M + \lambda K$$

where μ and λ are the constants of proportionality and M and K are the mass and stiffness coefficients. The stiffness coefficient is related to the damping coefficient through the following equation

$$M = 2\zeta\omega$$

The benefit of using a stiffness coefficient instead of a damping coefficient is that the stiffness coefficient assumes that the damping is linearly proportional to response frequency. Although this isn't always true, it is a good approximation for when the exact damping coefficient and frequency are unknown. In addition, the effect of the stiffness coefficient of the model was also compared in fig. 37 As can be seen, the lower the stiffness coefficient, the larger total energy output there will be in the system since there is an overshoot and oscillation in the system.

Figure 36. Voltage output with different stiffness coefficients at 60 MPH vs. time

RESISTANCE

Different resistance values were applied on the harvester to study the effect of resistance on voltage output. As depicted in fig. 37, the higher the resistance value, the larger the voltage. This is due to the extremely large internal resistance of the harvester. Note that the value of the voltage during impedance matching (calculated in Ch. 4) is almost the same as the open circuit voltage. This is because the impedance matching value's resistance should produce the maximum power.

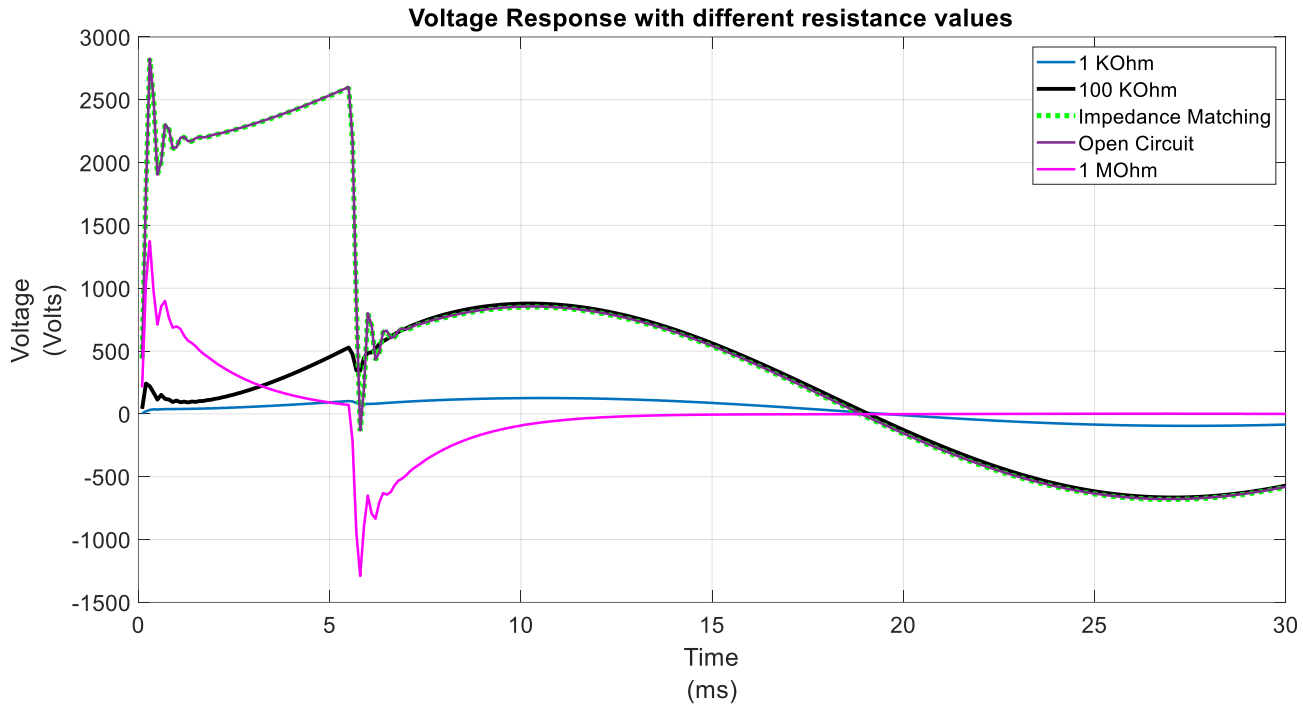

Figure 37. Voltage response with various resistances vs. time

1-5 MODE

Since the top part of the harvester is 15 mode, the polarization direction of the layers is parallel to the electrodes. Hence, the polarization can either be in the x or z directions. Therefore, a simulation of the harvester in each polarization direction was conducted. As illustrated in fig. 38 the x direction polarization generated a higher voltage.

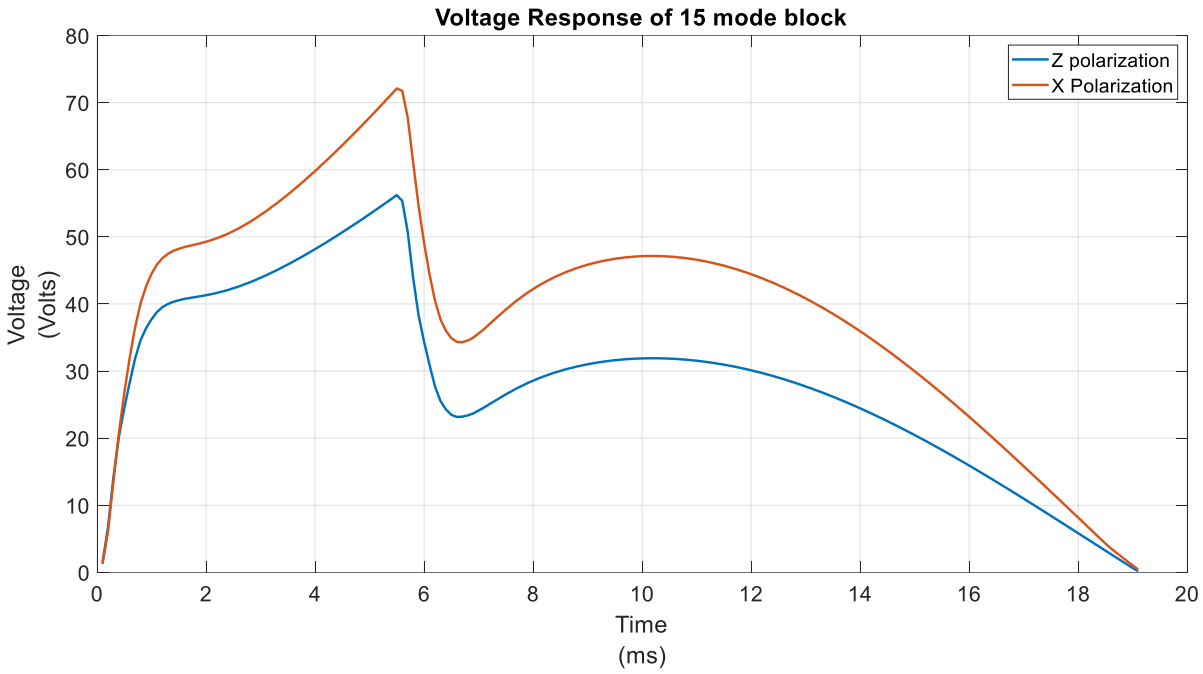

Figure 38. Voltage response of the top part of the harvester in different polarization directions vs. time.

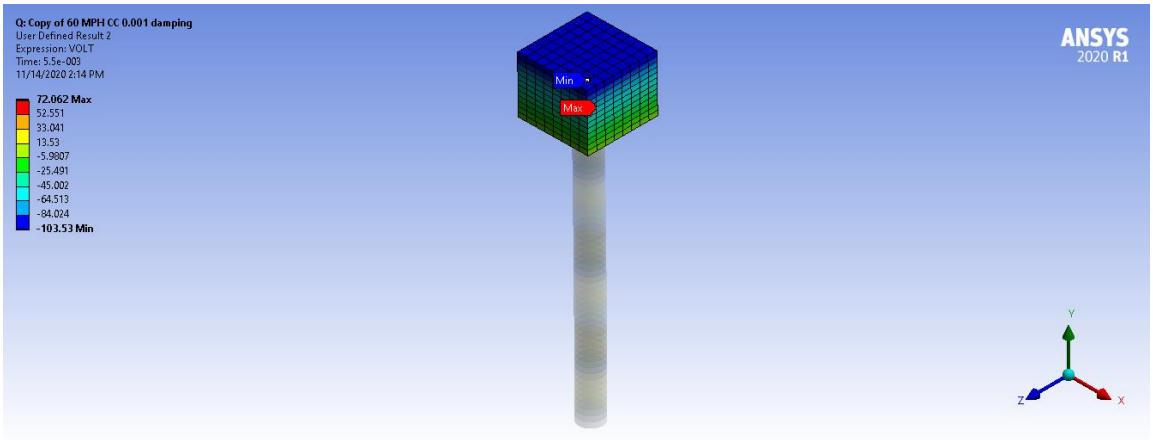

Figure 39. Contour plot of 15 mode block with polarization in the X-direction.

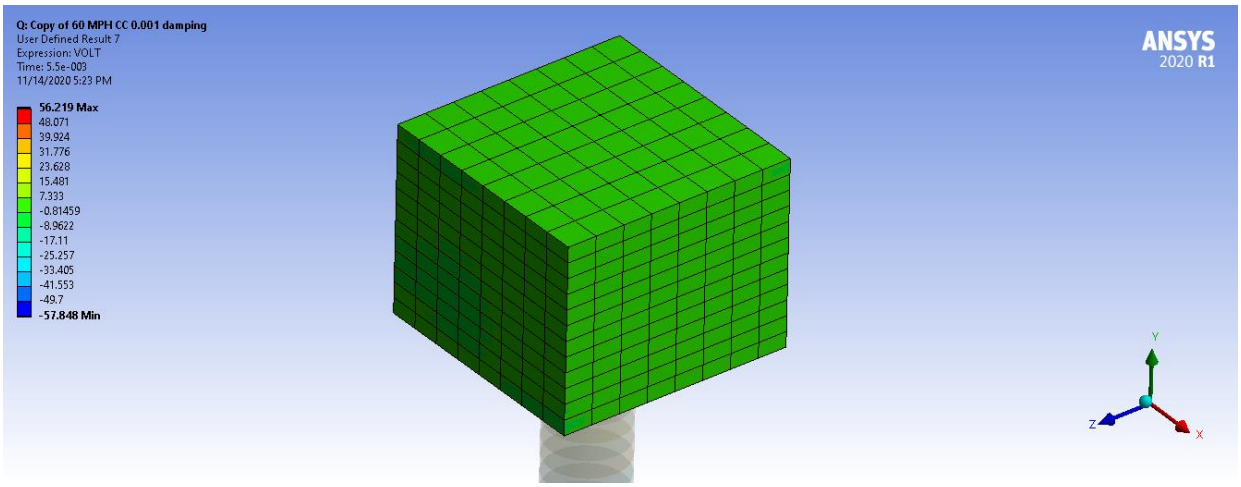

Figure 40. Contour plot of 15 mode block with polarization in the Z-direction.

VI. SUMMARY AND FUTURE WORK

An ultra-high-power density model for roadway applications based on a dual-mode piezoelectric generator was evaluated. Finite element analysis provided design guidelines to optimize power output and determine the structural integrity of the harvester when a vehicle passes over it. The design allows for multiple harvesters to be connected together in parallel. This offers unique advantages in terms of total power output. Precisely, the total power output scales linearly with the number of harvesters since each harvester is mechanically independent from the other based on the linear assumptions made during our modelling. The harvester generated a maximum RMS Power value of 1.29 W when the freight truck passed over it in the impedance matching closed circuit model. Furthermore, vehicle speeds of 25 MPH, 45 MPH, and 60 MPH were analyzed to determine the effect of speed on the voltage output. The slower the vehicle, the longer the contact duration which in turn, produces the highest energy output. The conditions that produced the highest voltage in the simulations ran had the parameters shown in table 10

Table 10: Simulation parameters used

Parameter	Value
$Stiffness\ Coefficient$	0.001
$Resistance$	$Z_{P_{Bottom}} = 3.8947 \times 10^7\ \Omega,$ $Z_{P_{TOP}} = 7.5179 \times 10^5\ \Omega$
$15 - mode\ polarization\ direction$	$X -\ Direction$
$Vehicle\ speed$	$25\ MPH$

In the future, this study can be extended to different designs to see which design is the most efficient. The effect of temperature on the harvester can also be evaluated since the harvester will be subjected to temperature differences due to changes in weather. Also, a dynamic load can replace the static load in order to create a more realistic simulation. Additionally, a feasibility study

must be conducted to determine which design has the highest Watt/dollar ratio. For the current design, the damping effect of the dirt on the harvester can be evaluated to replace the frictionless support. Furthermore, an experimental study with the actual model is a must since it will assist in pinpointing the main conditions that affect our system. Also, it will help determine the exact damping ratio of the harvester. Moreover, a cost benefit analysis to determine if the power output of the 15-mode block compared to the 33-mode bottom part can be conducted.

REFERENCES

[1] J. Curie, P. Curie, Développement par compression de l'électricité polaire dans les cristaux hémièdres à faces inclinées, Bull. La Société Minéralogique Fr. 3 (1880) 90–93. https://doi.org/10.3406/bulmi.1880.1564.

[2] M.G. Lippmann, Principle de la Conservation de l'électricité, Ann. Chim. Phys. 24 (1881) 381–394.

[3] W.G. Cady, Piezoelectricity : an introduction to the theory and applications of electromechanical phenomena in crystals, New York (N.Y.) : McGraw-Hill, 1946, 1946.

[4] R.S. Dahiya, M. Valle, Robotic tactile sensing: Technologies and system, 2014. https://doi.org/10.1007/978-94-007-0579-1.

[5] Utilizing Piezoelectricity and Photovoltaics to Increase Hybrid Car Efficiency, (n.d.).

[6] T. Nayyar, K. Pubby, S.B. Narang, R. Mishra, Energy harvesting using piezoelectric materials, 2016. https://doi.org/10.1080/10584587.2016.1252660.

[7] P. Paufler, Fundamentals of Piezoelectricity, Zeitschrift Für Krist. 199 (1992) 158–158. https://doi.org/10.1524/zkri.1992.199.1-2.158.

[8] K. Uchino, Piezoelectric actuators 2006, (2008) 301–311. https://doi.org/10.1007/s10832-007-9196-1.

[9] B. Jaffe, Piezoelectric Ceramics, 1971.

[10] T. Zheng, J. Wu, D. Xiao, J. Zhu, Progress in Materials Science Recent development in lead-free perovskite piezoelectric bulk materials, Prog. Mater. Sci. 98 (2018) 552–624.

https://doi.org/10.1016/j.pmatsci.2018.06.002.

[11] M. Karaki, T., Yan, K., Miyamoto, T., and Adachi, Lead-Free Piezoelectric Ceramics with Large Dielectric and Piezoelectric Constants Manufactured from BaTiO3 Nano-Powder JJAP Express Letter Lead-Free Piezoelectric Ceramics with Large Dielectric and Piezoelectric Constants Manufactured from BaTiO 3 Nano-P, 97 (n.d.) 97–99. https://doi.org/10.1143/JJAP.46.L97.

[12] S. Jaffe, B., Roth, R., and Marzullo, Piezoelectric Properties of Lead Ceramics, 809 (1954) 809–810. https://doi.org/10.1063/1.1721741.

[13] L.E. Cross, R.E. Newnham, History of Ferroelectrics, 111 (1987).

[14] L.E.A. Pautov, A.T.A. Agakhanov, FROM THE DARA-I-PIOZ ALKALINE MASSIF , NORTHERN TAJIKISTAN : DESCRIPTION AND CRYSTAL STRUCTURE after the Russian mineralogist Igor Viktorovich Pekov, 42 (2004) 107–119.

[15] B. Bhushan, Scanning Probe Microscopy in Nanoscience and Nanotechnology, 2010. https://doi.org/10.1007/978-3-642-03535-7.

[16] T.R. Shrout, Relaxor based ferroelectric single crystals for electro-mechanical actuators, 3 (1997) 20–25.

[17] T.R. Park, S. E. E., Vedula, V., Pan, M.-J., Hackenberger, W. S., Pertsch, P., and Shrout, Relaxor-based ferroelectric single crystals for electromechanical actuators, (1998). https://doi.org/10.1080/00150199808229559.

[18] S. Zhang, J. Luo, W. Hackenberger, T.R. Shrout, S. Zhang, J. Luo, W. Hackenberger, T.R. Shrout, ferroelectric crystal with enhanced phase transition temperatures crystal with

enhanced phase transition temperatures, 064106 (2013) 10–15. https://doi.org/10.1063/1.2978333.

[19] Z. Cheng, V. Bharti, T. Xu, H. Xu, T. Mai, Q.M. Zhang, Electrostrictive poly (vinylidene ¯ uoride-tri ¯ uoroethylene) copolymers, 90 (2001) 138–147.

[20] M. Shehzad, T. Malik, Antiferroelectric Behavior of P (VDF-TrFE) and P (VDF-TrFE-CTFE) Ferroelectric Domains for Energy Harvesting, (2018). https://doi.org/10.1021/acsaem.8b00478.

[21] J.S. Harrison, N. Langley, Piezoelectric Polymers, (2001).

[22] A. American, N. Standard, An American National Standard: IEEE Standard on Piezoelectricity, IEEE Trans. Sonics Ultrason. 31 (1984) 8–10. https://doi.org/10.1109/T-SU.1984.31464.

[23] S.P.A. Robert S. Anderson, Geomorphology. The mechanics and chemistry of landscapes, 17 (2011) 427–428.

[24] S. Bhagavantam, D. Suryanarayana, Crystal symmetry and physical properties: application of group theory, Acta Crytallographica. 2 (1949) 21–26. https://doi.org/10.1107/S0365110X49000047.

[25] D. Berlincourt, PIEZOELECTRIC CRYSTALS AND CERAMICS, (1971).

[26] K. Uchino, Materials, 2nd ed., Elsevier Ltd., n.d. https://doi.org/10.1016/B978-0-08-102135-4.00010-2.

[27] D. Paik, S. Park, T.R. Shrout, Dielectric and piezoelectric properties of perovskite materials at cryogenic temperatures, 4 (1999) 469–473.

[28] T. Xu, L. Tolliver, X. Jiang, J. Su, T. Xu, L. Tolliver, X. Jiang, J. Su, A single crystal lead magnesium niobate-lead titanate multilayer-stacked cryogenic flextensional actuator A single crystal lead magnesium niobate-lead titanate multilayer-stacked cryogenic flextensional actuator, 042906 (2013) 12–16. https://doi.org/10.1063/1.4790142.

[29] H. Yu, J. Zhou, L. Deng, Z. Wen, A Vibration-Based MEMS Piezoelectric Energy Harvester and Power Conditioning Circuit, Sensors. (2014) 3323–3341. https://doi.org/10.3390/s140203323.

[30] J. Baker, Alternative Geometries for Increasing Power Density in Vibration Energy Scavenging, (2005) 1–12.

[31] K. Uchino, Ferroelectric Devices, Second, 2018. https://doi.org/https://doi.org/10.1201/b15852.

[32] L. APC International, Piezoelectric Ceramics: Principles and Applications, APC Int. (2011).

[33] T.-B. Xu, Energy harvesting using piezoelectric materials in aerospace structures, in: Struct. Heal. Monit. Aerosp. Struct., 2016: pp. 175–212. https://doi.org/10.1016/B978-0-08-100148-6.00007-X.

[34] P. Heyliger, H. Ledbetter, S. Kim, Elastic constants of natural quartz, J. Acoust. Soc. Am. 114 (2003) 644–650. https://doi.org/10.1121/1.1593063.

[35] P. Sarafis, A.G. Nassiopoulou, Dielectric properties of porous silicon for use as a substrate for the on-chip integration of millimeter-wave devices in the frequency range 140 to 210 GHz, (2014) 1–8.

[36] R.A. Islam, S. Priya, Rashed Adnan Islam and Shashank Priya, 3156 (2006).

https://doi.org/10.1111/j.1551-2916.2006.01205.x.

[37] A. Hajati, Ultra Wide-Bandwidth Micro Energy Harvester, (2010).

[38] L. Luo, X. Zhao, H. Luo, Single Crystal PZN-PT, PMN-PT, PSN-PT, and PIN-PT-Based Piezoelectric Materials, 2nd ed., Elsevier, 2010. https://doi.org/10.1016/B978-0-08-102135-4.00007-2.

[39] J. Chen, R. Panda, Review : Commercialization of Piezoelectric Single Crystals for Medical Imaging Applications, 00 (2005) 235–240.

[40] A. Amin, E. Mclaughlin, H. Robinson, L. Ewart, Mechanical and Thermal Transitions in Morphotropic PZN-PT and PMN-PT Single Crystals and Their Implication for Sound Projectors, 54 (2007) 1090–1095.

[41] H.S. Nalwa, Ferroelectric Polymers Chemistry: Physics, and Applications, CRC Press, 1995.

[42] T.-B. Xu, Z.-Y. Cheng, T. Mai, Y. Lu, Q. Zhang, Electromechanical coupling factor of electrostrictive P (VDF-TrFE) copolymer, 2000 IEEE Ultrason. Symp. Proceedings. An Int. Symp. 2 (2000) 997–1000.

[43] T. Xu, J. Su, Design , Modeling , Fabrication , and Performances of Bridge-Type High-Performance Electroactive Polymer Micromachined Actuators, 14 (2005) 539–547.

[44] S. Priya, D.J. Inman, Energy harvesting technologies, 2009. https://doi.org/10.1007/978-0-387-76464-1.

[45] S. Roundy, P.K. Wright, A piezoelectric vibration based generator for wireless electronics, Smart Mater. Struct. 13 (2004) 1131–1142. https://doi.org/10.1088/0964-1726/13/5/018.

[46] Y. Sun, X. Gao, H. Wang, Z. Chen, Z. Yang, A wideband ultrasonic energy harvester using 1-3 piezoelectric composites with non-uniform thickness, Appl. Phys. Lett. 112 (2018) 1–5. https://doi.org/10.1063/1.5012822.

[47] H. Liu, J. Zhong, C. Lee, S.W. Lee, L. Lin, A comprehensive review on piezoelectric energy harvesting technology: Materials, mechanisms, and applications, Appl. Phys. Rev. 5 (2018). https://doi.org/10.1063/1.5074184.

[48] S. Roundy, P.K. Wright, J. Rabaey, A study of low level vibrations as a power source for wireless sensor nodes, 26 (2003) 1131–1144.

[49] P. Glynne-Jones, S.P. Beeby, N.M. White, Towards a piezoelectric vibration-powered microgenerator, IEE Proc. Sci. Meas. Technol. 148 (2001) 68–72. https://doi.org/10.1049/ip-smt:20010323.

[50] X. Gao, W. Shih, W.Y. Shih, X. Gao, W. Shih, W.Y. Shih, Vibration energy harvesting using piezoelectric unimorph cantilevers with unequal piezoelectric and nonpiezoelectric lengths Vibration energy harvesting using piezoelectric unimorph cantilevers with unequal piezoelectric and nonpiezoelectric lengths, 233503 (2014) 10–13. https://doi.org/10.1063/1.3521389.

[51] Y. Suzuki, Recent Progress in MEMS Electret Generator for Energy Harvesting, (2011) 101–111. https://doi.org/10.1002/tee.20631.

[52] Z. Wang, Y. Xu, Vibration energy harvesting device based on air-spaced piezoelectric cantilevers, Appl. Phys. Lett. 90 (2007) 3–6. https://doi.org/10.1063/1.2752726.

[53] S. Mehraeen, S. Member, S. Jagannathan, S. Member, K.A. Corzine, S. Member,

Scavenging Circuitry and Tapered Cantilever Beam, 57 (2010) 820–830.

[54] M. Shabara, T.-B. Xu, Comprehensive Piezoelectric Material Application Issues on Energy Harvesting for Artificial Intelligence Systems, in: American Institute of Aeronautics and Astronautics (AIAA), 2020. https://doi.org/10.2514/6.2020-1862.

[55] V.R. Challa, M.G. Prasad, Y. Shi, F.T. Fisher, A vibration energy harvesting device with bidirectional resonance frequency tunability, Smart Mater. Struct. 17 (2008). https://doi.org/10.1088/0964-1726/17/01/015035.

[56] W.J.C.Y. Jeon, J.J.R. Sood, Energy harvesting MEMS device based on thin film piezoelectric cantilevers, (2006) 543–548. https://doi.org/10.1007/s10832-006-6287-3.

[57] R. Wille, Karman vortex streets, Adv. Appl. Mech. 6 (1962) 273–287.

[58] M. Bryant, E. Garcia, Modeling and Testing of a Novel, 133 (2013). https://doi.org/10.1115/1.4002788.

[59] A. Abdelkefi, M.R. Hajj, Performance enhancement of wing-based piezoaeroelastic energy harvesting through freeplay nonlinearity, 041001 (2013) 4–7. https://doi.org/10.1063/2.1304101.

[60] H.D. Akayd, N. Elvin, Wake of a cylinder : a paradigm for energy harvesting with piezoelectric materials, (2010) 291–304. https://doi.org/10.1007/s00348-010-0871-7.

[61] J. Sirohi, R. Mahadik, Piezoelectric wind energy harvester for low-power sensors, 22 (2015) 2215–2228. https://doi.org/10.1177/1045389X11428366.

[62] L. Zhao, L. Tang, Y. Yang, Comparison of modeling methods and parametric study for a piezoelectric wind energy harvester, 125003 (n.d.). https://doi.org/10.1088/0964-

1726/22/12/125003.

[63] M.F. Daqaq, Modeling and Characterization of a Piezoelectric Energy Harvester Under Combined Aerodynamic and Base Excitations, 137 (2016) 1–12. https://doi.org/10.1115/1.4029611.

[64] H.W.O.O. Kim, S. Priya, K. Uchino, R.E. Newnham, Piezoelectric Energy Harvesting under High Pre-Stressed Cyclic Vibrations, (2005) 27–34.

[65] A. Abdelkefi, F. Najar, A.H. Nayfeh, S. Ben Ayed, An energy harvester using piezoelectric cantilever beams undergoing coupled bending-torsion vibrations, Smart Mater. Struct. 20 (2011). https://doi.org/10.1088/0964-1726/20/11/115007.

[66] M.A. Shabara, ENERGY HARVESTING USING FLEXTENSIONAL PIEZOELECTRIC ENERGY HARVESTERS IN RESONANCE AND OFF RESONANCE MODES, 2020.

[67] APC, PHYSICAL AND PIEZOELECTRIC PROPERTIES OF APC MATERIALS, (n.d.). https://www.americanpiezo.com/apc-materials/physical-piezoelectric-properties.html.

[68] R. Nave, Friction and Automobile Tires, (n.d.). http://hyperphysics.phy-astr.gsu.edu/hbase/Mechanics/frictire.html#:~:text=The friction between the tires,importantly your minimum stopping distance.&text=Jones and Childers report coefficients,an %22all weather%22 compromise.

[69] Ford F-150/F-250: How to Determine Proper Tire Pressure, (n.d.). https://www.ford-trucks.com/how-tos/a/ford-f150-f250-how-to-determine-proper-tire-pressure-355594.

[70] D. Tire, Understanding the Contact Patch, (n.d.). https://www.discounttire.com/learn/contact-patch.

[71] F. Qian, T.B. Xu, L. Zuo, Material equivalence, modeling and experimental validation of a piezoelectric boot energy harvester, Smart Mater. Struct. 28 (2019). https://doi.org/10.1088/1361-665X/ab1eb7.

[72] Y. Motola, L. Banks-Sills, V. Fourman, A note on tensile testing of poled and unpoled piezoelectric ceramics, Strain. 45 (2009) 85–92. https://doi.org/10.1111/j.1475-1305.2008.00477.x.

APPENDIX

APDL CODE

```
TIMINT, ON !Turns on transient effects
/PREP7 !Enters the model creation preprocessor
ET,2000,CIRCU94,0 ! Set up the bottom resistor
R,3000,2.7587e+09 ! Specify a value for the resistance

ET,2001,CIRCU94,0 ! Set up the top resistor
R, 3001, 5.3251e+07 !Specify a value for the resistance

N, 12000, 0, -3.95e-17,0.2 !Creates a node at the bottom surface
N, 12001, 0, 0.28, 0.2 !Creates a node at the top surface (cylinder)
TYPE,2000 $REAL,3000 !Sets the element type attribute pointer
E, 12000, 12001 !Create an element between both nodes

N,30002,0,0.34,0.3 !Creates a node at the top surface
N, 30001, 0, 0.28, 0.3 !Creates a node at the bottom surface
(Block)
TYPE,2001 $REAL,3001 !Sets the element type attribute pointer
E, 30001, 30002 !Create an element between both nodes

/SOLU !Enters the solution processor
NSEL,S, LOC,Y,-3.95e-17 !Selects a subset of nodes at a specific
location
cp,1000,volt, all !Applies a voltage coupling to the nodes
*GET, n_bot, node, 0, num, min !retrieves the minimum value of the
coupled elements
NSEL,ALL
```

```
NSEL,S, LOC,Y,0.34
cp,1500,volt, all
*GET, n_topblock, node, 0, num, min
NSEL,ALL

NSEL,S, LOC,Y,0.28
cp,2500,volt,all
*GET, n_top, node, 0, num, min
D,n_top,VOLT,0
NSEL,ALL
```

PUBLICATIONS

[1] Shabara, Mohamed, **Badawi, Abdul**, & Xu, Tian-Bing. (2020). Comprehensive Piezoelectric Material Application Issues on Energy Harvesting for Artificial Intelligence Systems. AIAA SciTech 2020 Forum

[2] Jovanovic, Vukica, Kuzlu, Murat, Popescu, Otilia, **Badawi, Abdul** et al**.** (2020). An Initial Look into the Computer Science and Cybersecurity Pathways Project for Career and Technical Education Curricula

[3] Hayajneh, Mohammad & **Badawi, Abdul**. (2019). A*utomatic UAV Wireless Charging over Solar Vehicle to Enable Frequent Flight Missions*. ICACR